

Accepted Manuscript

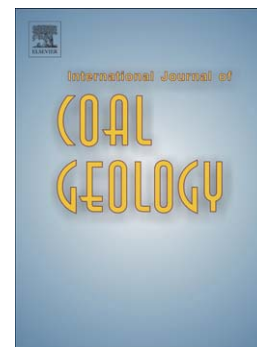
Sorption and changes in bulk modulus of coal – experimental evidence and governing mechanisms for CBM and ECBM applications

Sander Hol, Yves Gensterblum, Paul Massarotto

PII: S0166-5162(14)00094-9
DOI: doi: [10.1016/j.coal.2014.04.010](https://doi.org/10.1016/j.coal.2014.04.010)
Reference: COGEL 2292

To appear in: *International Journal of Coal Geology*

Received date: 24 February 2014
Revised date: 16 April 2014
Accepted date: 16 April 2014



Please cite this article as: Hol, Sander, Gensterblum, Yves, Massarotto, Paul, Sorption and changes in bulk modulus of coal – experimental evidence and governing mechanisms for CBM and ECBM applications, *International Journal of Coal Geology* (2014), doi: [10.1016/j.coal.2014.04.010](https://doi.org/10.1016/j.coal.2014.04.010)

This is a PDF file of an unedited manuscript that has been accepted for publication. As a service to our customers we are providing this early version of the manuscript. The manuscript will undergo copyediting, typesetting, and review of the resulting proof before it is published in its final form. Please note that during the production process errors may be discovered which could affect the content, and all legal disclaimers that apply to the journal pertain.

Sorption and changes in bulk modulus of coal – experimental evidence and governing mechanisms for CBM and ECBM applications

Sander Hol^{1,*}, *Yves Gensterblum*², *Paul Massarotto*³

¹ Stanford University, Department of Geophysics, 397 Panama Mall, Stanford, CA 94305-2115, United States

² RWTH Aachen University, Institute of Geology and Geochemistry of Petroleum and Coal, Lochnerstr. 4-20, 52056 Aachen, Germany

³ University of Queensland, School of Chemical Engineering, Brisbane, St Lucia 4067, Qld, Australia

*corresponding author: hol@stanford.edu

Abstract

Recent studies report that the stiffness of coal changes, when exposed to sorbing gases such as CH₄ and CO₂. Although this effect might be potentially important for predicting the *in situ* mechanical behavior of coal seams during CH₄ production or CO₂ sequestration, very little understanding exists on the underlying mechanisms. In this paper, we report a single, long-duration mechanical test on a large, cube-shaped coal sample (Ruhr Basin, Germany). The sample was subjected to isostatic loading and unloading; first in the evacuated state (as received), and then each time after exposing it to pressurized, non-adsorbing He, or sorbing N₂, CH₄, and CO₂. We find that exposure to sorbing gases led to swelling, which introduced a hysteresis in the stress-strain trajectory followed during mechanical loading. This hysteresis was almost absent in the evacuated state, and its magnitude depended strongly on the amount of adsorption-induced swelling exhibited by the sample. The apparent bulk modulus determined here for the CO₂-equilibrated state was approximately 25% lower compared to the evacuated state. We qualitatively consider mechanisms that affect the elastic behavior of coal at the matrix and bulk scale, and argue that the observed effects are a combined effect of 1) changes in surface roughness at cleat interfaces and microfractures, and 2) a thermodynamic coupling between stress state, sorption capacity and swelling strain. The changes in stiffness relate to fluid-rock interaction effects, as well as to the presence of fractures, and hence not to the inherent elastic properties of the solid phase itself. We discuss the characteristics of each mechanism and the connection of the proposed mechanisms with formation-scale geomechanical effects of coal layers under conditions relevant to CBM/ECBM.

1 Introduction

Accurate predictions of CH₄ production rates and the CO₂ sequestration potential of coal reservoirs rely heavily on understanding of the physical-chemical processes that operate under *in situ* conditions. An important feature uniquely observed in such systems is the strong competition between adsorption-related effects and poroelasticity (e.g. Hol and Spiers, 2012; Liu et al., 2011; Palmer and Mansoori, 1998; Pan and Connell, 2007; Vandamme et al., 2010; White et al., 2005), and between fluid dynamics and poroelasticity (Gensterblum et al., 2013a). Despite the many laboratory and modeling studies that have been reported in the literature to date, the manner in which these processes affect formation-scale geomechanics remains difficult to understand. In this paper, we aim to separate and describe direct mechanisms and feedback effects that influence the mechanical response of coal under *in situ* conditions of isostatic stress and fluid pressure, in particular the recoverable response that is expected to influence transport properties. We relate these mechanisms to the properties of the solid phase and changes in these due to the sorbing nature of N₂, CH₄ and CO₂, at various scales.

The bulk modulus of the solid, coal matrix framework can be determined using ultrasonic velocity measurements (dynamic tests). Morcote et al. (2010) and Schuyer et al. (1954) performed experiments on multiple coal core plugs, and showed that tangent bulk moduli systematically increase with coal rank. Values are typically in the range 2-12 GPa and show only slight dependence on confining pressure (Morcote et al., 2010; Schuyer et al., 1954). Static (mechanical) tests performed on core-scale samples show tangent bulk moduli in the range 0.5-15 GPa. These values are typically non-linearly dependent on stress state (e.g. data of Gentzis et al., 2007). Mechanically determined bulk moduli are generally lower at applied stresses in the range 0-10 MPa because of the added compliance introduced by the presence of cleats and fractures at the cm-scale. This effect is well-known in rock mechanics and applies to many other rock types (Cook, 1992; Zimmerman, 1985; Zisman, 1933). At stress levels above 10 MPa, or with sufficiently consolidated and crack-free samples, the tangent moduli obtained using the dynamic versus static methods will be close, as is for example the case in for results reported by Hagin and Zoback (2010) for coal cores of one inch in diameter from the Powder River Basin, USA.

Recent papers, however, report that the exposure of both low and high rank coal samples to CH₄ or CO₂ changes both the bulk stiffness (De Silva and Ranjith, 2012; Hagin and Zoback, 2010; Masoudian et al., 2013; Ranjith and Perera, 2012; Viete and Ranjith, 2006) as well as the matrix stiffness (Hol et al., 2011, 2012a; Lwin, 2011). Interestingly, all studies using mechanical data reported a reduction of stiffness relative to virgin-state measurements (De Silva and Ranjith, 2012; Hagin and Zoback, 2010; Hol et al.,

2011, 2012a; Ranjith and Perera, 2012; Viete and Ranjith, 2006), whereas dynamic tests reveal no change (Hagin and Zoback, 2010) or an increase in stiffness (Lwin, 2011). Because static moduli are calculated on the basis of external stress-strain data, and dynamic moduli on the basis of ultrasonic wave propagation through the solid phase, these observations clearly point in the direction of multiple scale-dependent processes operating in coal-adsorbate systems. The reduction in stiffness observed in static tests has been explained by “adsorptive weakening” or plasticization processes activated by the presence of CH₄/CO₂ in the coal skeleton (De Silva and Ranjith, 2012; Viete and Ranjith, 2007), or alternatively by a direct coupling between stress state, sorbed concentration and swelling strain (Hol et al., 2011, 2012a). By contrast, the stiffening observed in the dynamic tests has been explained by local compression of the solid framework in the coal matrix, caused by an excess pressure generated in the sorbing phase in the nanopores (Lwin, 2011). Note that the latter stiffening mechanism clearly disagrees with the idea of plasticization, which involves “softening” of the solid framework.

All mechanisms mentioned above operate at the matrix-scale, whereas the mechanical response to changes in stress and fluid pressure at the bulk-scale is undoubtedly affected by the presence of cleats, fractures and heterogeneous bedding. The scope of this paper is on the feedback effects introduced by these features, and their role in coupling the matrix-scale to bulk-scale mechanical response of coal. This is poorly understood at present, while at the same time crucial for the upscaling to a geomechanical framework at the reservoir scale.

We report a single, long-duration mechanical test performed on a cube-shaped coal sample measuring 80x80x80 mm; this size is sufficient to contain 8 to 10 cleats in each orthogonal, bedding-intersecting direction, and is a good representation of the *in situ* cleat density. The work reported here is the result of a collaborative experimental program involving RWTH Aachen University, Stanford University, and the University of Queensland (related reports by Massarotto et al., 2010; Wang et al., 2007; Wang et al., 2010), and focused on the mechanical response and permeability evolution of coal in CBM/ECBM reservoirs. We subjected the sample to mechanical loading and unloading using a polyaxial compaction cell, first in the evacuated state, and then each time after exposing it to either helium, or sorbing N₂, CH₄, and CO₂. The stress conditions applied during the experiment were isostatic ($\sigma_1=\sigma_2=\sigma_3$), up to 12 MPa effective stress ($\sigma_e=\sigma_i-P_f$), and were close to the isostatic stress levels present under *in situ* conditions for the sample tested here. By choosing this procedure of cyclic loading/unloading in the evacuated and fluid-equilibrated state, we are able to systematically separate elastic and plastic components of deformation of the sample, consider their absolute magnitudes and relate these to mechanisms that operate on the large scale versus the matrix-scale, including the role of sorbing fluids such as N₂, CH₄ and CO₂. We discuss

the characteristics of the mechanisms proposed here, as well as the expected implications of their operation on the depletion and saturation behavior of coal layers under *in situ* conditions relevant to CBM/ECBM.

ACCEPTED MANUSCRIPT

2 Methods

We carried out a long-duration mechanical experiment on a single, cube-shaped coal sample. We subjected the sample to cyclic loading/unloading under evacuated and pressurized, N_2 -, CH_4 - and CO_2 -equilibrated conditions. Using fluid pressure, 3D strain, stress and fluid composition data, we investigate the effect of sorbing fluids on the mechanical response of our sample.

2.1 Sample origin, preparation and excess sorption characteristics

We used a specimen of a large block of high volatile bituminous coal sample extracted from the German Pennsylvanian (Upper Carboniferous, depth 915 m) in the Prosper Haniel Mine, Ruhr Basin, Germany. The sampled block had an overall vitrinite reflectance of 0.93%, a fixed carbon content of $58.4 \pm 0.8\%$, and a volatile matter content of $31.2 \pm 0.4\%$. Maceral group analysis revealed that the coal contained 69.8% vitrinite, 11.8% liptinite and 7.8% inertinite. Mineral matter, mainly in the form of pyrite and carbonate, constituted 11% of the sample volume. The carbonates were present as distinct horizons in the bedding plane. The cleat system and bedding plane were oriented perpendicular to each other. Helium pycnometry showed that the sample had a skeletal density of $1.36 \pm 0.03 \text{ g}\cdot\text{cm}^{-3}$. Comparing this with a bulk density of $1.25 \pm 0.01 \text{ g}\cdot\text{cm}^{-3}$ measured externally on the sample shows that the internal helium-accessible porosity of the sample was of the order of 8.5%. Inherent moisture content was $3.0 \pm 0.2\%$ (Table 1).

A cube-shaped specimen of 80x80x80 mm was cut from the large, intact sample using a diamond-powder covered sawing blade. The faces of this cube were reasonably parallel and smooth, at least in accordance with relevant standards developed by the International Society of Rock Mechanics (ISRM). It was made sure that the face-and-butt cleat system was oriented roughly parallel to the cube faces, so that mechanical loading of the sample could be achieved in directions normal to the face cleat, butt cleat and bedding planes. Fig. 1 shows an image of the sample obtained using CT-scanning techniques, and clearly shows the orthogonal set of cleats, as well as the bedding that includes carbonate horizons. After cutting, the near-perfect cube was neither dried, nor pre-exposed to any gases. The experiment was performed on the sample in “as received” condition, with an inherent moisture content of $3.0 \pm 0.2\%$.

Location	Basin	Lithostratigraphic Units	Age	Seam	Vit.Ref.	Rank
Prosper Haniel mine Germany	Ruhr basin	Westphalia B	Pennsylvanian	K	0.93	high volatile bituminous
Vitrinite reflectance				0.93 %		
Maceral group analysis						
Vitrinite				69.8%		
Liptinite				11.8%		
Inertinite				7.4%		
Mineral Matter				11% (Pyrite and Carbonate)		
Fixed carbon content				58.4 ± 0.8 %		
Volatile matter				31.2 ± 0.4 %		
Ash content				7.3 ± 2.2 % mainly Pyrite and Carbonates		
Inherent moisture content				3.0 ± 0.2 %		
Sample density						
Skeleton density				1.36 ± 0.03 g cm ⁻³		
Bulk density				1.25 ± 0.01 g cm ⁻³		
Pore system						
Helium-derived porosity				8.5%		
DR Micropore volume				3.2 10 ⁻² cm ³ g ⁻¹		

Table 1. Specific sample properties of the Prosper Haniel sample used in this study. Listed are details of the origin, maturity, maceral and mineral composition, and porosity.

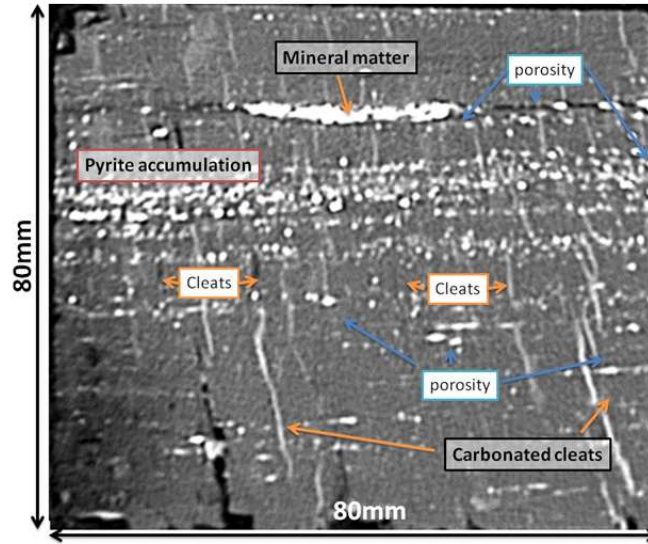


Fig. 1. CT image of a single face of the cube-shaped Prosper Haniel sample (vertical profile), prepared for this study. Note the accumulation of pyrite and carbonate material in the cleats and bedding plane. Cleat spacing was approx. 5-10 mm.

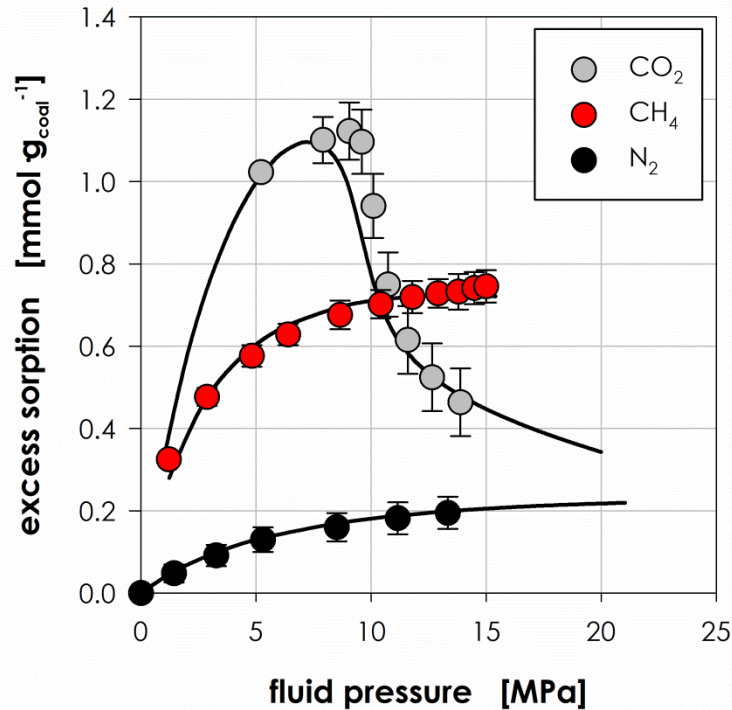


Fig. 2. N₂, CH₄ and CO₂ excess sorption isotherms for Prosper Haniel High Volatile Bituminous Coal. The tests were performed up to ~16 MPa fluid pressure at a temperature of 45 °C, using 7.2 g of a 0.177-1 mm sized grain fraction for the CH₄ test and 7.411g of a 0.5-1 mm sized grain fraction for the CO₂ test. The excess sorption isotherms were constructed using the manometric sorption method, as previously employed by Gensterblum *et al.* (2010; 2009) and Busch *et al.* (2003), and parameterized using a Langmuir fit.

In addition to the mechanical experiments performed on the large sample, manometric sorption tests were performed on crushed particles sampled from the intact block, using the same set-up as reported by Gensterblum et al. (2010; 2009) and Busch et al. (2003). This was done to demonstrate the potential role of adsorption in the mechanical response of the Prosper Haniel coal sample during our main mechanical test. Our tests were performed using N₂, CH₄ and CO₂ up to ~16 MPa fluid pressure (P_f) and at a temperature of 45 °C (318 K). Details on the experimental set-up can be found in the studies by Gensterblum et al. (2010; 2009) and Busch et al. (2003). Excess sorption characteristics are plotted in Fig. 2. These demonstrate that, at the fluid pressure condition of the mechanical experiment reported in this study ($P_f=3.0$ MPa) the excess sorption capacity of the sample is approx. 0.12 mmol·g_{coal}⁻¹ for N₂, 0.48 mmol·g_{coal}⁻¹ for CH₄, and 0.76 mmol·g_{coal}⁻¹ for CO₂ (Fig. 2). However, note that the temperature of manometric testing was 45 °C, compared to room temperature during the mechanical test. Also note, that the manometric tests were performed on crushed samples, instead of the large cube, the obtained excess sorption isotherms likely represent the absolute maximum excess sorption capacity under unconfined conditions. Finally, note that recent studies report that only small quantities of water in the coal structure affect the CH₄ and CO₂ sorption characteristics (Busch and Gensterblum, 2011; Gensterblum et al., 2014; Gensterblum et al., 2013b) and swelling response (van Bergen et al., 2009) of coal matrix material. Recognizing that the manometric and the mechanical testing conditions and procedures are different, we assume the relative magnitudes of sorption capacities (N₂:CH₄:CO₂ ≈ 1:4:6) obtained here to be representative for those under test conditions.

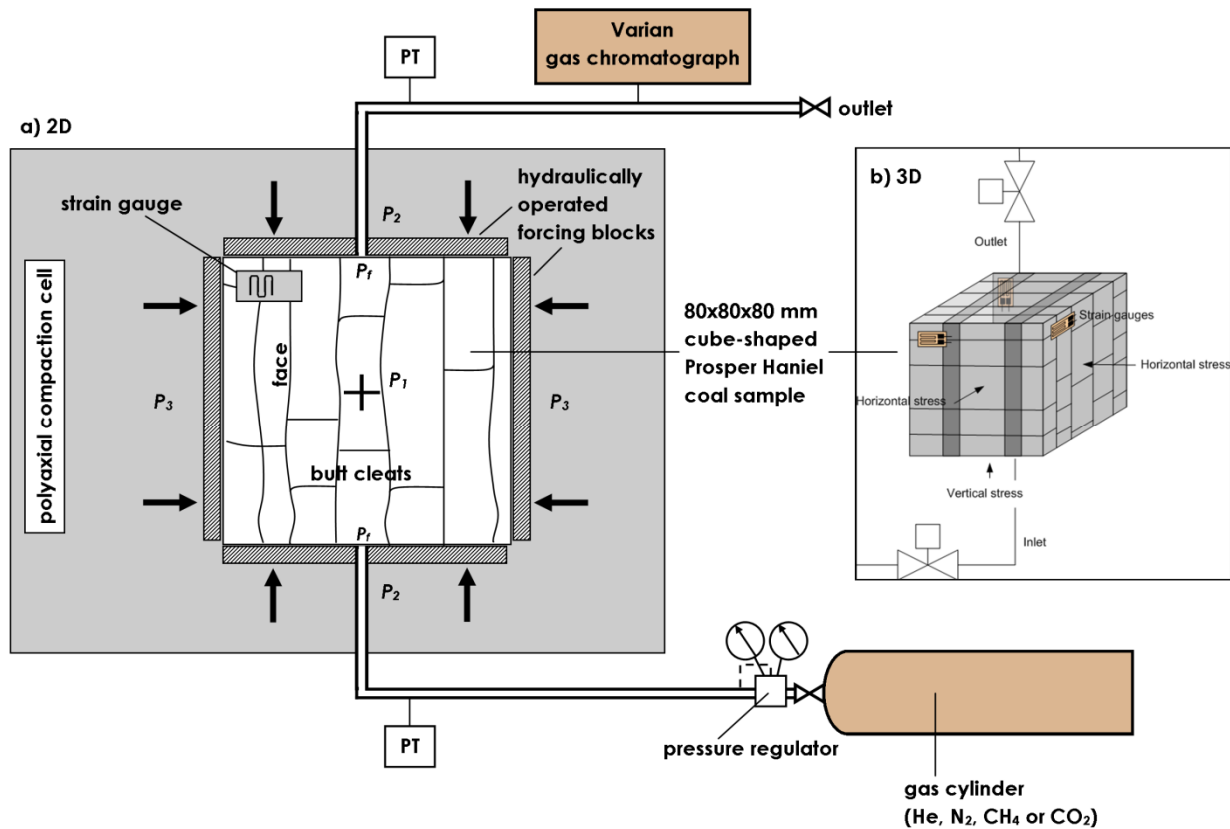


Fig. 3a) Schematic two-dimensional drawing of the polyaxial machine used to deform the Prosper Haniel sample at isostatic effective stresses up to 12.5 MPa. The sample (top view) was sealed in a polyurethane jacket (not specifically shown). Applied hydraulic pressures, $P_1(=\sigma_1)$, $P_2(=\sigma_2)$ and $P_3(=\sigma_3)$, and fluid pressure P_f were measured using Druck PTX 1400 pressure transducers. Isostatic stress (for $\sigma_1=\sigma_2=\sigma_3$) was applied in a stepwise manner, while maintaining a constant fluid pressure P_f of 3 MPa using He, N₂, CH₄ and CO₂. The system is located in an air conditioned facility ($RT=25^\circ\text{C}\pm 1.5^\circ\text{C}$), at the School of Engineering, University of Queensland, Brisbane, Australia. Please refer to Section 2.2.1, and to Massarotto et al. (2010), Wang et al. (2007) and Wang et al. (2010) for further details. b) Three-dimensional drawing of sample, showing the arrangement of strain gauges. Note, that the right-side plane is the in situ top of the sample.

2.2 Experimental set-up and procedure

2.2.1 Polyaxial compaction cell and fluid pressure system

In order to measure the 3D strain response of the 80x80x80 mm, cube-shaped coal sample during isostatic loading in the evacuated and fluid-equilibrated state, we used a high-pressure, hydraulically operated polyaxial (or “true-triaxial”) compaction cell (Fig. 3). This type of compaction cell was chosen because of its ability to hold large, cube-shaped samples. This shape better matches the 3D cleat-ply structure of

coal, and hence allows to couple the 3D strain data to the directional, structural properties of the bulk sample, as it responds to underground 3D stress fields. Technical details on the polyaxial system were reported earlier by Massarotto et al. (2010), Wang et al. (2007) and Wang et al. (2010).

Stress can be applied to the sample in three mutually orthogonal directions independently up to a maximum of 28 MPa stress, mechanically applied at each face of the 80x80x80 mm cube. However, we here employed the machine under isostatic conditions only (*i.e.* $\sigma_1=\sigma_2=\sigma_3$). The pressure of the hydraulic fluid was measured using Druck PTX1400 pressure transducers (60 MPa high range), located in the hydraulic fluid lines, and was measured with an accuracy of ± 0.12 MPa. Sealing of the sample from any external confining fluids is achieved by means of a thick, single piece skeleton jacket, composed of polyurethane rubber (Fig. 3).

The pore fluid system was connected to inlet and outlet ports of the cell, and the relative sample and cell positioning such that fluids could be introduced to the sample directly in the face cleat plane direction. Evacuation of the sample could be achieved by means of the connected lab vacuum system (Fig. 3). Gas pressure P_f was measured by Druck PTX1400 pressure transducers (10 MPa high range), located at both the inlet and outlet side of the cell, with an accuracy of ± 0.02 MPa. The mean pressure (being an average of inlet and outlet measurements) was calculated as the basis of permeability and effective stress calculations (following Terzaghi: $\sigma_e = \sigma_{isostatic} - P_f$). When performing fluid displacement tests using two components at constant pressure (e.g. when displacing CH₄ by injecting CO₂), the composition of the produced fluids was determined using a Varian CP-3900 micro gas chromatograph (GC) and Thermal Conductivity Detector (TCD) located at the downstream end of the fluid pressure system (Fig. 3). The GC was externally sourced by helium as a carrier gas. Note, that this excluded the possibility to determine helium concentrations in the outflow gas.

Dimensional changes of the sample, in response to the changes in fluid pressure and external stresses, were measured using three sets of strain gauges, each fixed to a face of the cube, yielding strains in the face cleat, butt cleat and vertical planes. The size of the strain gauges was 9x5 mm, and hence less than the cleat spacing of 10 to 25 mm for the range of HVB coals. The gauges are attached using epoxy glue, into 2mm-deep recesses in fixed locations opposite cell outlets. The strain gauges were obtained from Micromeritics-Vishay (Model CEA-06-125UN120), and were calibrated to be accurate within approximately 0.1% linear strain.

Temperatures are measured by transducers upstream and downstream, but were not actively controlled, as all tests were carried out at an air conditioned room temperature of $25\text{ }^{\circ}\text{C} \pm 1.5^{\circ}\text{C}$. However, the actual measured mean temperature is used for gas flow and permeability calculations only.

2.2.2 *Stepwise isostatic loading of sample in the evacuated versus fluid-saturated state*

The cube-shaped sample was inserted into the polyurethane jacket, with all faces of the sample, and hence the face cleat, butt cleat and bedding planes, oriented normal to the direction of the loading pistons. Immediately following installation, the sample was evacuated for 2 h. In the case of loading after evacuation, (quasi non-adsorbing) helium was introduced at atmospheric pressure, and the sample was loaded stepwise from 0.1 MPa to 10 MPa isostatic effective stress (Terzaghi) in ~ 1 MPa increments, and then unloaded to ~ 0.1 MPa. This was done three times to assess recoverability and reversibility of the sample deformation. The strain response was recorded for each face of the cube to assess strain anisotropy, and hence the anisotropy in elastic properties. Note, that we will use the term “evacuated” throughout this paper to indicate that the sample has been evacuated, and is exposed to (quasi non-adsorbing) helium at atmospheric pressure only.

After loading the sample in the evacuated state, the sample was sequentially exposed to pressurized helium, N_2 , CH_4 and CO_2 , with pressure increased after each saturation stage. All gas exposure stages in our experiment are therefore performed at a fluid pressure of 3 MPa, and an isostatic effective stress of 6 MPa.

First, helium as an essentially non-adsorbing gas was introduced to the sample by connecting the pressure cell directly to the gas bottle, and the gas pressure was regulated at 3 MPa. Then, a loading cycle was performed in a stepwise manner, at effective stress levels between 3 and 12.5 MPa, with quasi-regular 1 MPa intervals. Then, N_2 was flushed through the sample, again at a pressure of 3 MPa, to displace the helium. During the gas displacement steps in which no helium was involved, aliquots of the outflow gas were sampled each 80 sec and injected into the Varian GC and TCD to determine the composition of the outlet fluid. Dimensional changes were measured at all times using the strain gauges. When the relative concentrations measured by the GC indicated that sufficient equilibration was achieved, stabilization of at least another 24 h was allowed to reach a swelling equilibrium (observed by leveling off of strain gauge readings). Once the sample was equilibrated, it was again loaded to 12.5 MPa effective stress, and then unloaded to 6 MPa. The procedure of flushing and loading-unloading was then performed with the equilibration steps $\text{N}_2 \rightarrow \text{CH}_4$, and $\text{CH}_4 \rightarrow \text{CO}_2$. For all fluids, the loading cycles took about 6-10 h, and involved a stepwise increase of the confining stress up to 12 MPa effective stress. Strain, effective stress

and fluid pressure data were recorded with 14 bit resolution, at 1 min intervals. Strains are presented relative to the dimensional state at the onset of the first loading cycle in the evacuated state. Volumetric strains are calculated as the sum of all linear (directional) strains following the simple relation

$$\varepsilon_v = \varepsilon_{\text{vert}} + \varepsilon_{\text{fc}} + \varepsilon_{\text{bc}}$$

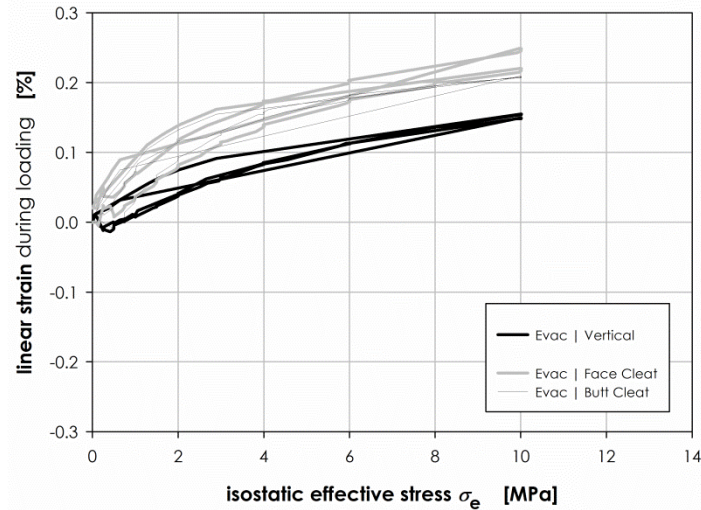


Fig. 4. Linear strain versus isostatic effective stress for the cube-shaped Prosper Haniel coal sample in the evacuated state. Data were obtained from strain gauge measurements and resolved for the vertical, face cleat and butt cleat directions.

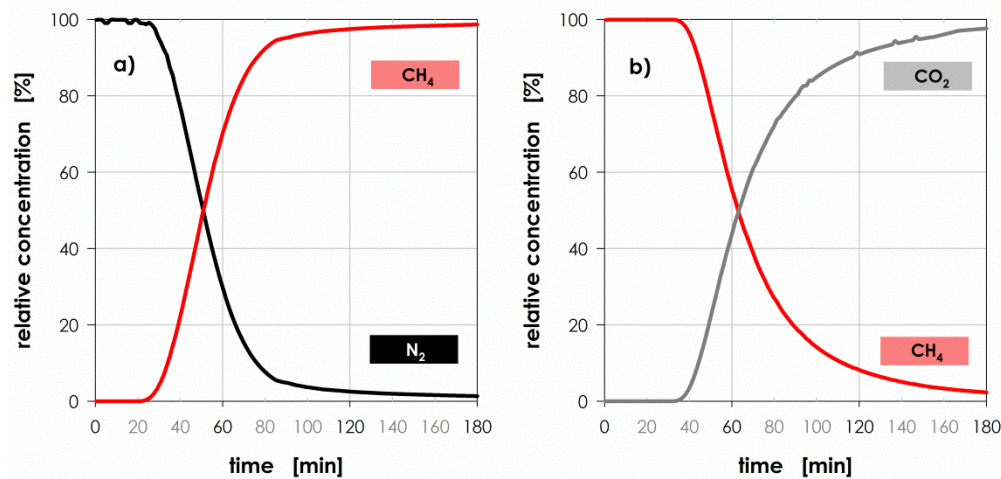


Fig. 5. Relative concentrations of CH_4 , CO_2 and N_2 during gas displacement steps as obtained via the Varian GC located at the outlet of the pore pressure system. Note the s-shaped concentration profile, showing that the displacement in connected void system of N_2 by CH_4 , and CH_4 by CO_2 was effectively achieved in approximately 3 hr.

3 Results

Bulk linear strain data recorded during the loading cycles performed in the evacuated state (helium at atmospheric pressure present in the pores) are presented in Fig. 4. Relative gas concentrations at the outflow during gas displacement are presented in Fig. 5. Swelling strains are presented in Fig. 6, and strains recorded during loading of the sample in the fluid-equilibrated state in Fig. 7 through Fig. 9. Incremental strains recorded during the fluid-equilibrated loading stages of the experiment were plotted as a function of a) isostatic effective stress (Fig. 7 and Fig. 8), b) cumulative swelling strain (Fig. 9), and c) time (Fig. 10). Throughout, we adopt the convention that compression strain is measured positive.

3.1 Strain data evacuated state

Loading of the evacuated Prosper Haniel sample (Fig. 4) resulted in a monotonic, non-linear increase of volumetric strain up to $\sim 0.6\%$ at 10 MPa of isostatic effective stress. Approximately 50% of the total strain was attained below 3 MPa effective stress. A comparison of the three loading cycles performed shows that all strains were recoverable and reversible to within 0.03-0.05% (linear) or 0.1% (volumetric), which points towards sufficient mechanical (elastic) integrity of the sample. The linear strain data for the faces of the 8 cm coal cube show that most strain was attained in the bedding directions, indicating a strongly anisotropic response. The general trend observed in the volumetric strain versus effective stress data is similar to the data for the individual measurement directions, i.e. the vertical, face cleat and butt cleat strain data all show that approximately 50% of the strain was attained below 3 MPa effective stress. Strains recorded on the face-cleat plane were generally twice as large compared to the vertical strains. Tangent bulk moduli of the sample varied between ~ 1 GPa at the onset of loading and ~ 3.2 GPa in the range 6-10 MPa isostatic effective stress, indicating ~ 3 times stiffer behavior at close to *in situ* stress conditions.

3.2 Fluid equilibration and swelling

After performing the multiple, full loading-unloading cycles in the evacuated state, He, N₂, CH₄ and CO₂ were passed through the sample in sequence, at 3 MPa fluid pressure. Fig. 5 shows the relative concentrations of displaced fluids at the outlet of the sample during the gas displacement at 3 MPa fluid pressure. As pointed out earlier, the Varian GC used helium as a carrier gas, and hence the release of the experimental helium could not be determined. The concentration profiles shown in Fig. 5 are s-shaped,

for both the displacement stages N_2 to CH_4 (Fig. 5a) and CH_4 to CO_2 (Fig. 5b). Both curves were cut off at 180 min. The slope of the concentration profile around the inflection point decreases with increasing sorptive interaction of the gas species with the coal material, i.e. the slope decreases in the order $N_2 > CH_4 > CO_2$. Consistent with this, also the breakthrough time increases in the same order (Table 2). A close examination of the concentrations in the full data set (i.e. times later than 180 min - not presented) showed an asymptotic evolution of the relative concentrations. Furthermore, the displacement of CH_4 by CO_2 resulted in the continued release of less than 1% of residual N_2 . This could point at slow outgassing of residual sorbed/trapped gas.

Gas displacement	Breakthrough beginning time t_B (c<5%) (s)	End of breakthrough t_E (c>95%) (s)	dc/dt concentration change during breakthrough (1/s)	t_0 breakthrough time (s)
He by N_2	1499	4697	0.050 ± 0.0010	1370 ± 44
N_2 by CH_4	1832	5255	0.043 ± 0.0003	1863 ± 21
CH_4 by CO_2	2414	8607	0.033 ± 0.0006	2260 ± 62

Table 2. Breakthrough times for gas-to-gas displacements; first order parameterization of the breakthrough curve. Prior to t_B , the outlet solute concentration is less than the arbitrary limit of 0.05. At t_B , this value is reached, and the adsorption step should be discontinued. If the adsorption step were to be continued for $t > t_B$, the outlet solute concentration will rise rapidly, eventually approaching the inlet concentration as entire bed become saturated. The time required to reach $C_{out}/C_F = 0.95$ is designated t_E . Using a linear regression around the inflection point (25% up to 75%) of the concentration curve of the displacing gas. Slope (third column) is a reciprocal coefficient representing relative interaction strength between the coal matrix and the two (competing) gases. The x-axis interception provides the theoretical start breakthrough time t_0 .

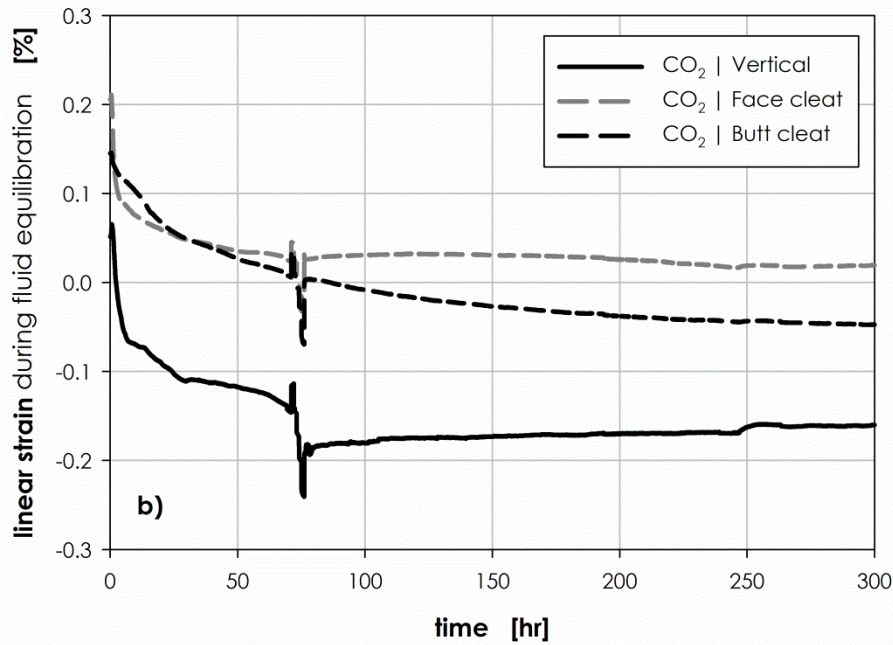
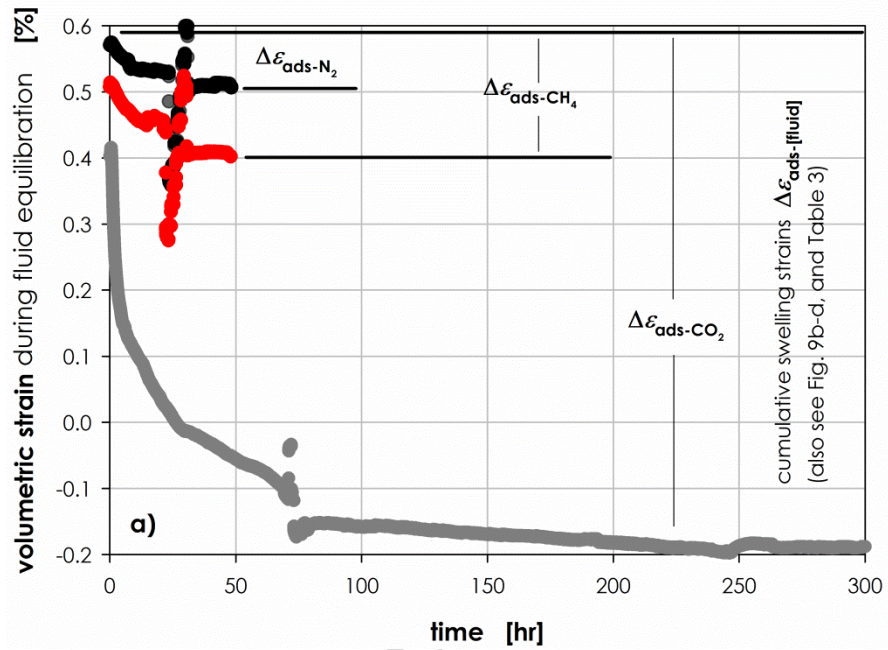


Fig. 6. Cumulative swelling strain versus time in hr during equilibration with N_2 , CH_4 , and CO_2 , interrupted by short episodes of active loading. a) Cumulative volumetric swelling strain evolving in the sample in 50 hr for the cases of N_2 and CH_4 , and 300 hr for the case of CO_2 . At approximately 75% of the maximum (asymptotic) swelling strain, a loading cycle was performed at 3 MPa gas pressure (see Fig. 7d); b) Linear strain response of sample equilibrated with CO_2 . Note the stronger swelling response in the direction perpendicular the bedding.

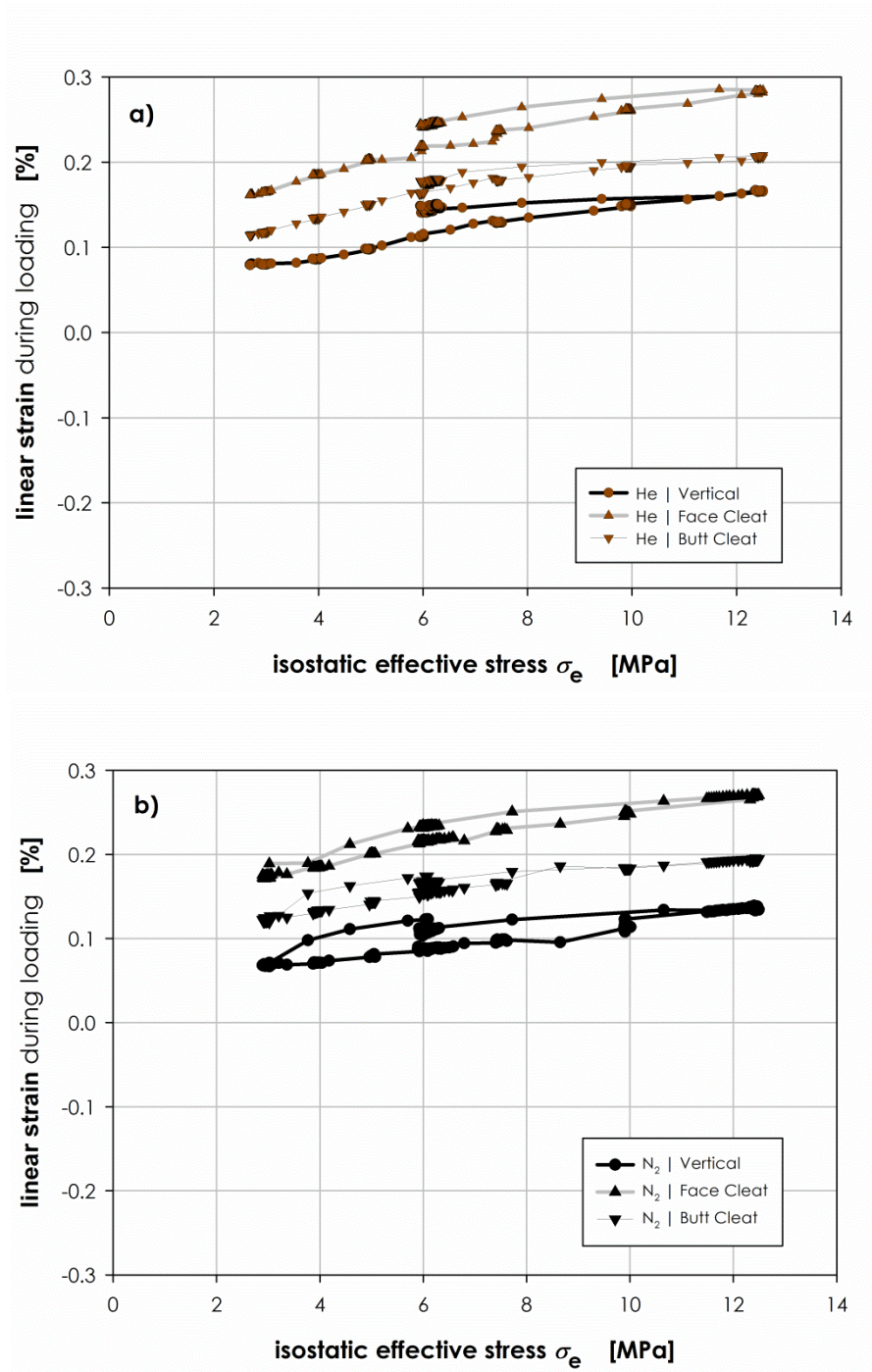
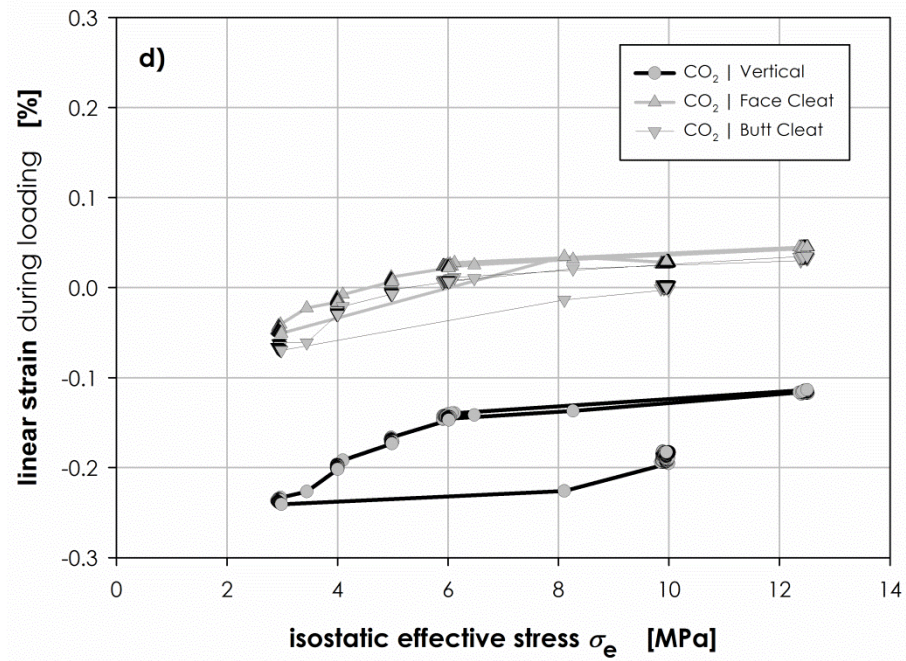
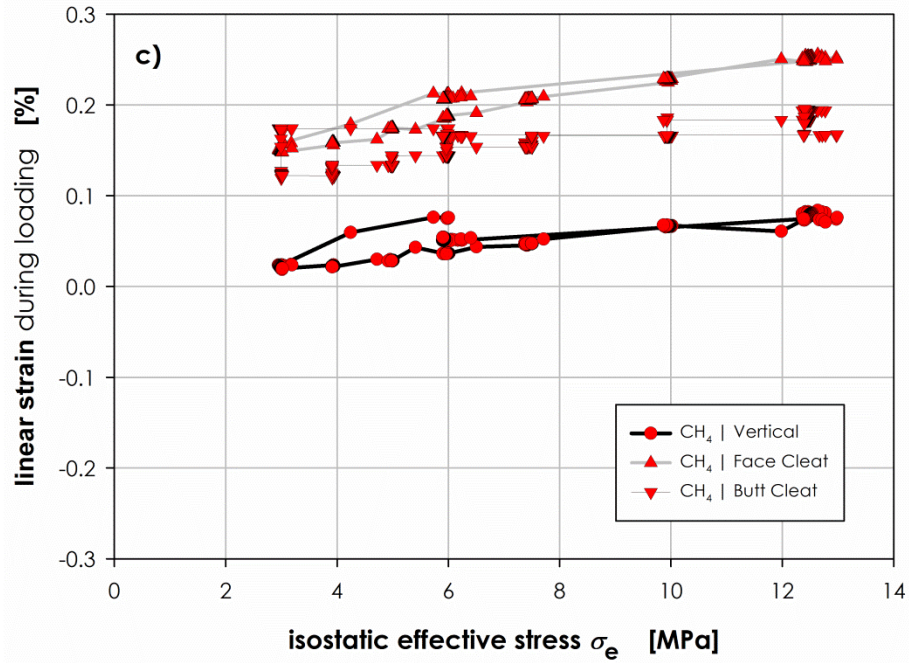


Fig. 7a-d. Linear strains versus isostatic effective stress for the cube-shaped Prosper Haniel coal sample in an ~75 % fluid-equilibrated state. Strain data were obtained from strain gauge measurements and resolved for directions perpendicular to the vertical, face cleat and butt cleat planes. Note the anisotropy in strain response, and hence stiffness of the sample.



Exposure of the sample to N_2 , CH_4 and CO_2 at 3 MPa fluid pressure and 6 MPa isostatic effective stress, resulted in a monotonic decrease of volumetric strains (i.e. swelling) (Fig. 6a). When approximately 75% of the final volumetric swelling strain was achieved, a relatively rapid isostatic loading-and-unloading cycle was performed (see Section 0). The strain data in Fig. 6a show that swelling continued after the loading cycle until a new asymptotic value was reached. All strains are reported as cumulative, because sorbing gases are displacing each other in sequence, at constant fluid pressure. Total cumulative swelling strains $\Delta\varepsilon_{ads-[fluid]}$, i.e. the strains attained relative to 0.58% measured strain when loaded to 6 MPa isostatic effective stress, were -0.08% for N_2 , -0.19% for CH_4 and -0.76% for CO_2 (Fig. 6a). Note again, that these strains are reported negative as a consequence of the sign convention chosen here (refer to Section 3). With this assumption, the swelling strains measured after gas displacement with CO_2 were 4 times greater than those measured with CH_4 . Moreover, swelling equilibration took 10-100 times longer than the gas displacement monitored by the Varian GC (compare Fig. 5 showing 3 hr flow-through and Fig. 6a showing 30-300 hr swelling).

Fig. 6b plots the directional strains for CO_2 , presented relative to the dimensional state at the onset of the first loading cycle in the evacuated state. The relative position of the directional curves can also be taken as qualitatively representative for the swelling behavior observed for N_2 and CH_4 . The data show anisotropy in the swelling strain response, both in magnitude as well as duration. The magnitudes of the swelling strains developed in the face and butt cleat direction are both in the order of approx. -0.2%, whereas the vertical strain is approx. -0.4%. By contrast strain evolution is relatively fast in the face cleat direction (approx. 50 hr), but slower in the butt cleat direction (200-300 hr) (Fig. 6b).

3.3 Strain data fluid-equilibrated state

Linear strains measured during active loading and unloading of the sample in the fluid-equilibrated state are presented in Fig. 7, and volumetric strains in Fig. 8. The data reveal trends roughly similar to those observed for the evacuated case (Fig. 4 and Section 3.1). Again, a monotonic, non-linear increase of volumetric strains with increasing isostatic effective stress can be observed in both the directional (Fig. 7) and volumetric strain (Fig. 8) curves. However, several important differences can be observed in mechanical behavior of the sample in the evacuated versus the fluid-equilibrated state. To highlight these, we follow the general procedure presented in Fig. 9a to determine the magnitude of total strains attained during loading in each cycle, i.e. the total vertical strain $\Delta\varepsilon_{vert}$, and total bedding-parallel strains $\Delta\varepsilon_{fc}$ (face cleat) and $\Delta\varepsilon_{bc}$ (butt cleat), determined on the basis of linear strains plotted in Fig. 7. We also estimate from Fig. 8 the apparent bulk modulus K_{app} over the stress interval tested, as well as the magnitude of the

hysteresis in volumetric strain $\Delta\epsilon_{\text{hyst}}$ during loading. Finally, we consider the time-dependent aspects during loading presented in Fig. 10. Using the obtained parameters $\Delta\epsilon_{\text{vert}}$, $\Delta\epsilon_{\text{fc}}$, $\Delta\epsilon_{\text{bc}}$ and $\Delta\epsilon_{\text{hyst}}$, four differences in mechanical response can be observed between the evacuated and the fluid-equilibrated cases.

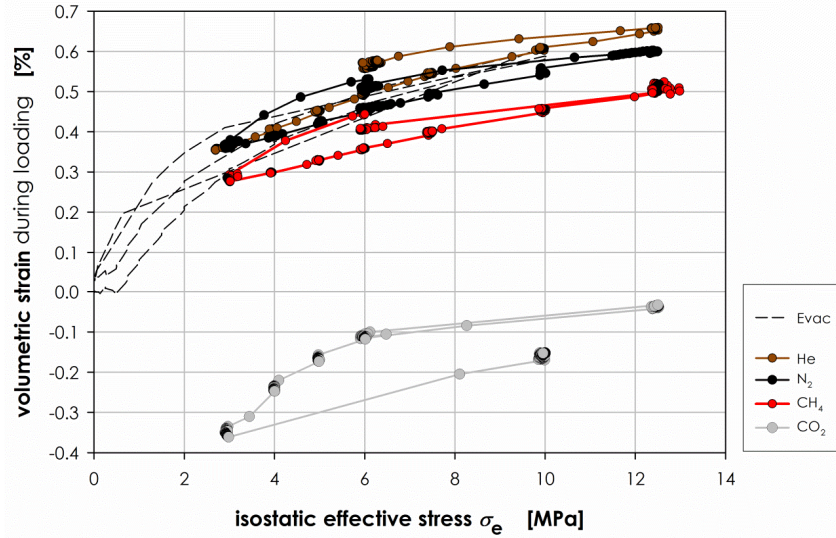


Fig. 8. Volumetric strains versus isostatic effective stress for the cube-shaped Prosper Haniel coal sample resolved from the linear strain plotted in Fig. 7. Compare the magnitudes of the loading hysteresis for each loading curve, as well as the effect of swelling on the volumetric state.

Gas	Excess adsorption at 3 MPa fluid pressure n_{excess} [mmol·g _{coal} ⁻¹]	Cumulative swelling strain $\Delta\epsilon_{\text{ads-[fluid]}}$ [%]	Strain anisotropy ratio [%]	Hysteresis volumetric strain [%]	Apparent bulk modulus K_{app} [GPa]
Evacuated	-	0.00	0.3182	-	
He	-	0.00	0.4000	0.060	3.68
N ₂	0.12	-0.09	0.4643	0.070	3.96
CH ₄	0.48	-0.19	0.4375	0.065	3.65
CO ₂	0.84	-0.76	0.6667	0.150	2.79

Table 3. Excess sorption and cumulative swelling strain values after equilibration for different gases used in the experiment. The strain anisotropy ratio, hysteresis in volumetric strain and apparent bulk modulus were determined following the procedure explained in Fig. 9a, and are plotted versus swelling strain in Fig. 9b-d.

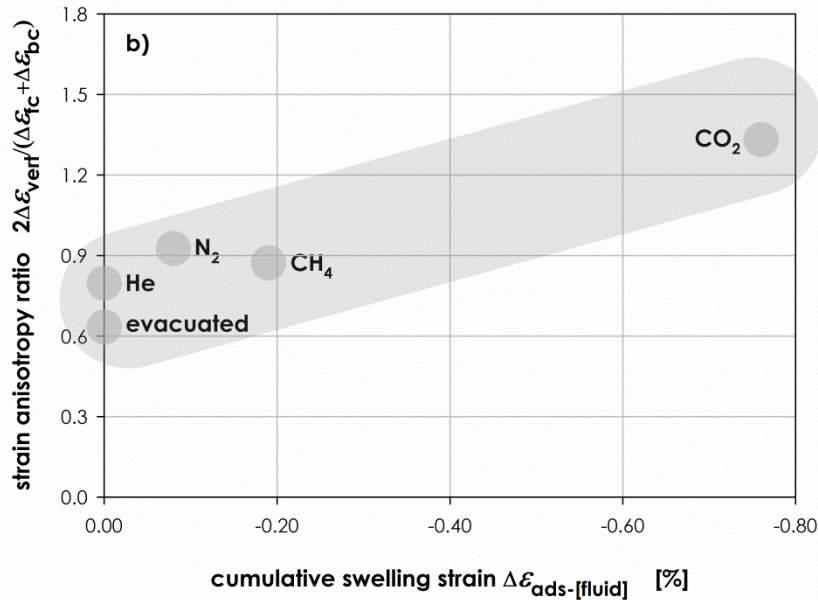
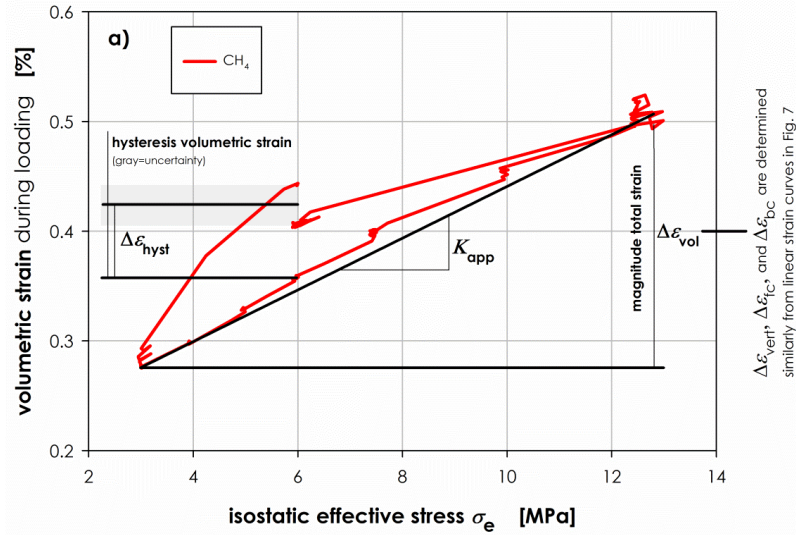
First, we calculate the strain anisotropy ratio as the total vertical strain over the mean bedding-parallel strain ($2\Delta\varepsilon_{\text{vert}}/(\Delta\varepsilon_{\text{fc}}+\Delta\varepsilon_{\text{bc}})$ – from Fig. 9a and Fig. 7), and plot in Fig. 9b this ratio against the total swelling strain $\Delta\varepsilon_{\text{ads}}$ for the individual fluids (from Fig. 6). This was done for each fluid, and is listed in Table 3. We now compare the points for the various fluids Fig. 9b) and find that the strain anisotropy increases as the sample has experienced more swelling, i.e. the increasing trend shown in Fig. 9b qualitatively shows that vertical strains are dominating compaction increasingly more with increasing swelling. The swelling, in turn, is strongly dependent on the type of fluid used. For the sorbing fluids N_2 , CH_4 and CO_2 , the magnitude of loading-induced strain is the greatest in the vertical direction. This is clearly in contrast with the response observed in the evacuated state, where the bedding plane was most compliant (compare Fig. 4).

Second, we plot in Fig. 9c the hysteresis in volumetric strains ($\Delta\varepsilon_{\text{hyst}}$) for the fluid-equilibrated state as function of the total swelling strain $\Delta\varepsilon_{\text{ads}}$ accumulated in the sample after equilibration with the individual fluids (Fig. 6). The closely linear trend observed in Fig. 9c clearly shows that increasing swelling results in larger strain hysteresis during loading and unloading. We make an important note here. The example data for CH_4 presented in Fig. 9a show that the strain-stress loop is not completely closed. In all cases, strains after the loading and unloading cycle were lower compared to the strains before. This ‘mismatch’ is at least partly related to ongoing swelling of the sample during the approximately 10 hours the loading took. At the same time, we observe that the magnitude of this swelling-related mismatch in strain is smaller than the strain hysteresis itself. On this basis, we are confident that the trend observed in Fig. 9c is not related to lack of equilibration, but instead to the true volumetric behavior of the sample during loading.

Third, the stiffness of the sample appears to decrease during the course of the experimental series. The apparent bulk modulus K_{app} of the sample was determined following the procedure presented in Fig. 9a for the sample equilibrated with all gases and yielded values of 3.68 GPa for helium, 3.96 GPa for N_2 , 3.65 GPa for CH_4 , and 2.79 GPa for CO_2 (Table 3 and Fig. 9d). From these results it is clear that exposure of the coal sample to CO_2 gives rise to 25% more compliant behavior compared to exposure to helium.

Finally, we present in Fig. 10 volumetric strain as a function of time for the all four different fluid-equilibrated loading cycles. We observe that for most loading steps in case of helium, N_2 and CH_4 , strain was achieved almost instantaneously. By contrast, CH_4 at higher stresses, and CO_2 throughout, clearly show time-dependent expansion and compaction. Note, the presence of a time-dependent strain response that is most pronounced for CO_2 . The CO_2 strain data (Fig. 10d) show that the stepwise reduction in

isostatic effective stress from 6 MPa to 3 MPa gives rise to time-dependent expansion. Loading to the highest applied isostatic effective stress of 10 MPa, on the other hand, results in a time-dependent compression of the order of approximately 0.02 % (Fig. 10d). The N₂ loading curve shows similar behavior, although smaller in magnitude. Unfortunately, the applied effective stress was too unstable to be conclusive on the reliability of this small effect.



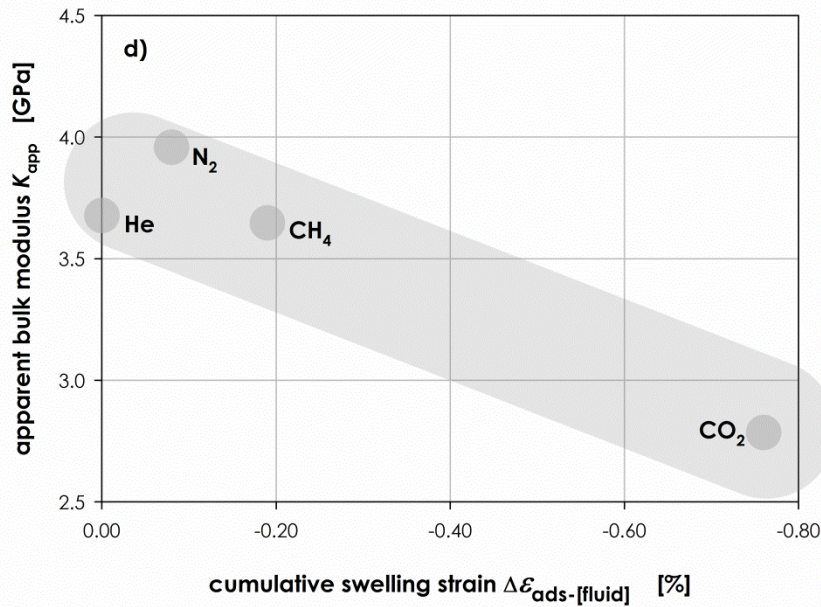
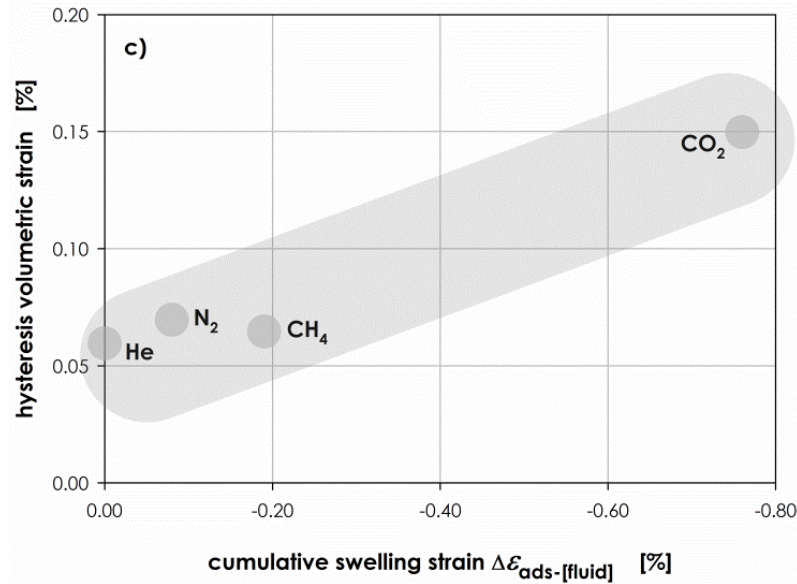


Fig. 9. Relationship between magnitude/hysteresis volumetric strain during loading and magnitude of swelling strain. a) Volumetric strain versus isostatic effective stress for loading sample in CH₄ equilibrated state showing definition of the magnitude of the strain hysteresis $\Delta\epsilon_{\text{hyst}}$ during loading and magnitude total strain $\Delta\epsilon_{\text{vol}}$. b) Relationship between strain hysteresis $\Delta\epsilon_{\text{hyst}}$ and cumulative swelling strain $\Delta\epsilon_{\text{ads}}$. Note the positive correlation between the amount of swelling strain attained and the strain anisotropy. c) Relationship between hysteresis in the volumetric strain strain $\Delta\epsilon_{\text{hyst}}$ and cumulative swelling strain $\Delta\epsilon_{\text{ads}}$. Note the positive correlation between the amount of swelling strain attained and the strain anisotropy. d) Relationship between apparent bulk modulus and cumulative swelling strain.

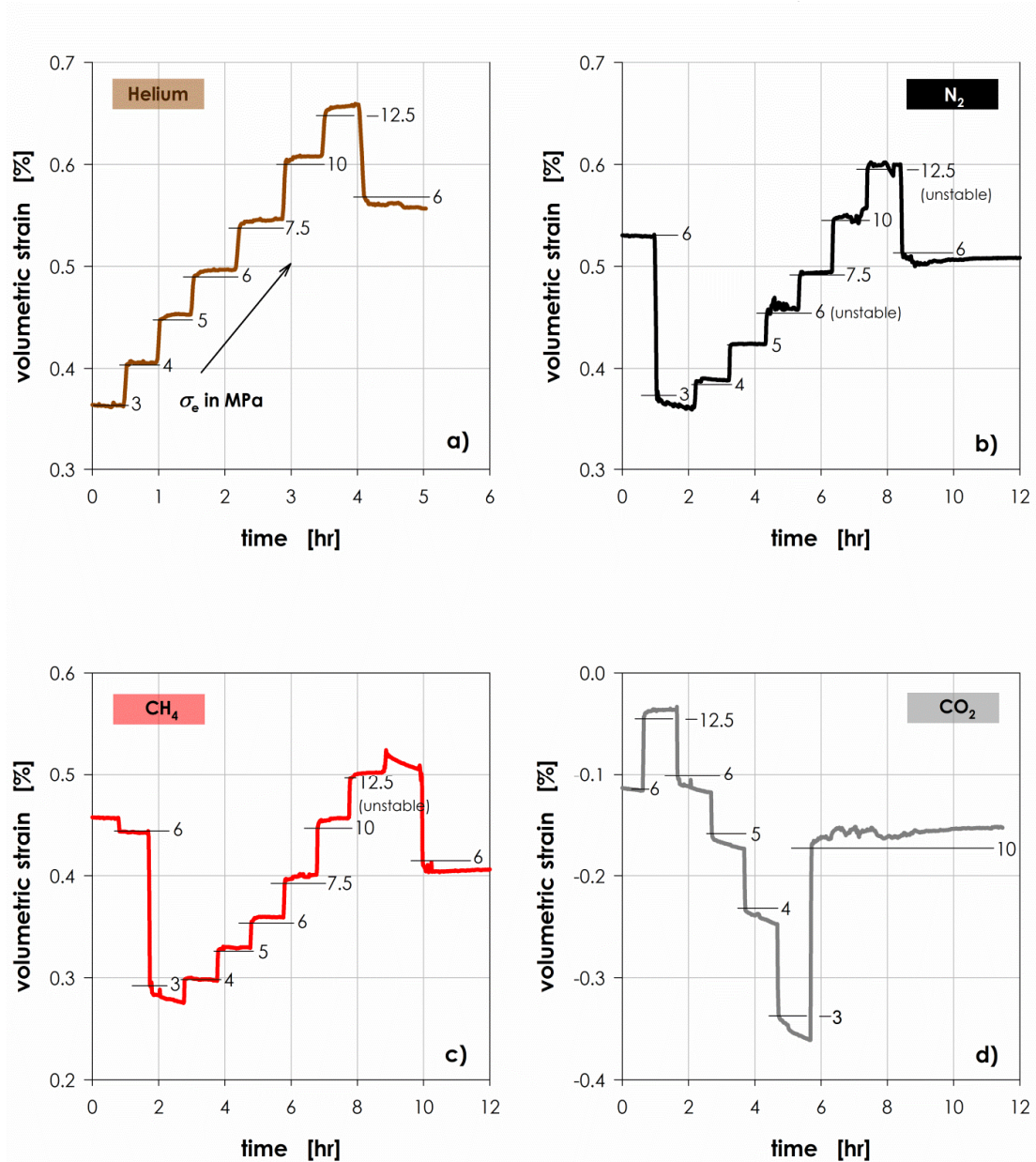


Fig. 10. Volumetric strains for cube-shaped Prosper Haniel coal sample versus time in hr, for four different gases applied during testing.

4 Discussion

4.1 Strain recoverability Prosper Haniel coal

Our stress-strain data showed that cyclic loading and unloading of the sample in the evacuated state resulted in non-linear, recoverable compaction, with a maximum strain of 0.6%. Exposure of the sample to He, N₂, CH₄ and CO₂, at 3 MPa fluid pressure and 6 MPa isostatic effective stress, lead to a subsequent swelling which depended strongly on the type of fluid sorbed (max. 0.05% for N₂ and 0.7% for CO₂). Although loading and unloading of the sample in the each fluid-equilibrated state resulted in a roughly similar recoverable strain response, the stress-strain trajectory followed in each case was characterized by a strong hysteresis. The hysteresis in our mechanical data (observed in Fig. 7 through Fig. 8) is of the type commonly observed in uniaxial loaded, fractured rocks (i.e. irreversible, but closely recoverable - David et al., 2012; Jaeger et al., 2007; Walsh, 1965), but also in the case of isostatic loading of anisotropic rocks (see Skurtveit et al., 2012 for a North Sea shale sample exposed to brine). Furthermore, a comparison of the magnitude of apparent bulk moduli obtained here with the bulk moduli obtained through ultrasonic velocity measurements (Morcote et al., 2010; Schuyer et al., 1954) yield relatively low values both in the evacuated and fluid-equilibrated states. The observed hysteresis in the stress-strain trajectory, combined with the relatively low bulk moduli, suggest that deformation in both the evacuated and fluid-saturated state is primarily concentrated in cleats and fractures, and not the solid phase. For the evacuated case, the strain response in the bedding direction is approx. 60-65% higher compared with strains in the direction perpendicular to the bedding (Fig. 4). Also, strains in bedding direction exhibit strong non-linearity as a function of stress. This provides additional support for the suggestion of a cleat-related elastic response.

Isostatic loading of the cube-shaped Prosper Haniel sample in the evacuated state also resulted in anisotropic compaction. Strains recorded on the face-cleat plane were generally twice as large as the vertical strains. The fracture-related strain anisotropy observed for the evacuated case is clearly in contrast with the behavior observed in the fluid-equilibrated state. Here, the strain hysteresis observed was greatest in the vertical direction, and depended strongly on the amount of adsorption-induced swelling exhibited (Fig. 9c). Although moduli were low in both the evacuated and fluid-equilibrated states, this swelling-related anisotropy suggests that the hysteresis in the fluid-equilibrated state bears a direct relationship not only with pre-existing cracks or cleats, but also with the adsorption processes itself that is operative in the matrix. Combining all directional strain components into a volumetric strain, shows that the sample exhibits up to 25% lower apparent bulk moduli in the fluid-equilibrated state, *i.e.* the stiffness of our bulk coal sample was reduced by exposure to sorbing fluids (Fig. 9d).

4.2 Changes in bulk stiffness related to adsorption

Dual porosity, single permeability reservoir simulators generally represent contacts between swelling matrix blocks (cleats) as non-tortuous, zero-volume discontinuities with a stress-dependent “cleat” compressibility (Connell et al., 2010; McKee et al., 1988; Shi and Durucan, 2004). Although this assumption proves highly practical in representing fluid flow through cleats, it does not account for direct changes in mechanical response during fluid depletion and re-saturation.

Our results show that the stiffness of bulk coal material reduces when exposed to sorbing fluids, which is in qualitative agreement with observations reported by other authors. However, a limited number of satisfactory thermodynamic or mechanical explanations have been proposed. In this section, we will discuss the possible cause of the bulk stiffness reduction and will consider two, scale-dependent classes of mechanisms and their physical characteristics. By using appropriate theoretical/thermodynamic expressions, we will demonstrate that these mechanisms can indeed lead to a change of coal stiffness at the bulk scale. Focusing on the relative importance of the physical behavior under *in situ* conditions, we finally consider some aspects of upscaling, and the relevance of this to CBM/ECBM operations.

4.2.1 Mechanism 1: Changes in surface roughness at cleat interfaces and microfractures (cleat- and bedding-scale)

Overall, the mechanical data presented here, in particular in Fig. 9b and Fig. 9c, suggest that horizontal strains become relatively less dominant in the volumetric strain response after equilibration with sorbing gases. Mechanisms causing the change in strain response (and hence bulk stiffness) are therefore expected to be related to the different role fractures play in the stiffness perpendicular to the bedding plane versus that parallel to it. Following, we will discuss these two directions separately.

In the bedding-parallel (horizontal) direction, the stiffness of the sample is clearly determined by the presence of cleats. In order to explain how this cleat-related stiffness is affected by the concentration of sorbed gas, we first need to understand the basic relationship between swelling strain, sorbed CO₂ concentration and cleat density of coal in general under unconfined conditions, separated from poroelastic effects. To do this, we utilize swelling strain data reported in the literature, and plot these against sorbed concentration. Fig. 11a presents an example of volumetric strain data, experimentally obtained by Day et al. (2008) on unconfined samples at increasing gas pressure, plotted against sorbed CO₂ concentration. We solely plot these data to explain the procedure we follow to establish a relationship between swelling

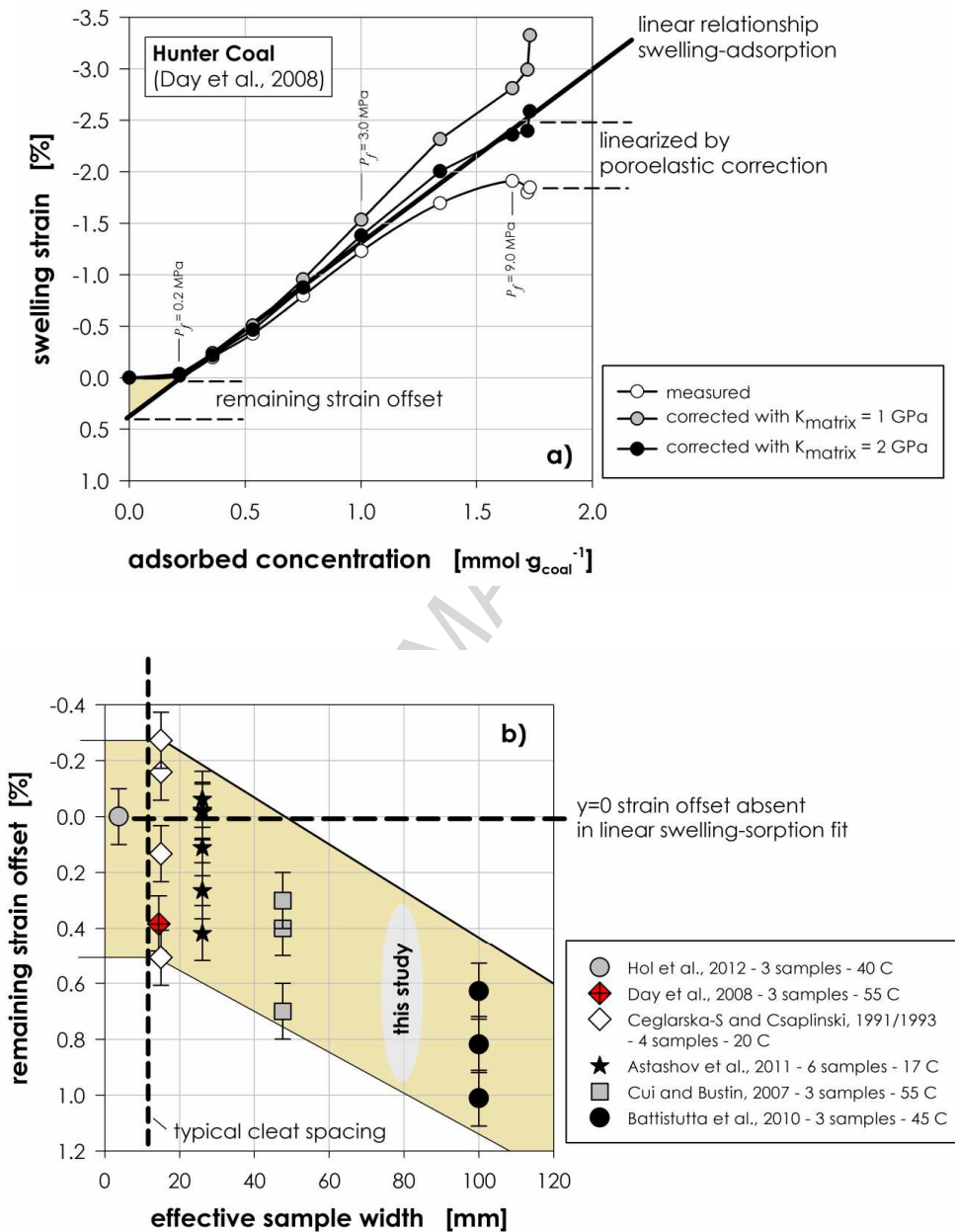


Fig. 11. a) Volumetric strain, experimentally obtained by Day et al. (2008), versus sorbed CO₂ concentration. Measured data are presented using white dots. Note, the s-shaped dependence of swelling on CO₂ concentration, and the three concentration-dependent domains of strain. Data corrected for poroelastic compression are presented using black/grey dots. The intercept of the linear swelling-adsorption fit with the y-axis, the remaining strain offset, is taken as a measure for a low-pressure non-linearity. b) Remaining strain offset versus the effective sample width (i.e. the cube root of the sample volume) for various data sets obtained from the literature. Error bars indicate worst case errors related to poor fitting and non-linearities resulting from parameterization of the literature data. Note larger remaining offsets for bigger samples, suggesting an effect of cleat density on measured swelling strain.

strain and cleat concentration based on literature data, and not to suggest a certain relation between the Hunter coal (Day et al., 2008) and the Prosper Haniel coal tested here. The measured strains plotted in Fig. 11a (white circles) show an s-shaped dependence on CO₂ concentration, which suggests three concentration-dependent domains of strain are manifested in the sample. The change in slope is greatest, and most linear, at sorbed concentrations between 0.2 and 1.1 mmol·g_{coal}⁻¹. Above 1.1 mmol·g_{coal}⁻¹, the slope gradually decreases until flattening at ~1.7 mmol·g_{coal}⁻¹. This effect is recognized by other authors, and is attributed to superposition of adsorption-induced and poroelastic strains (Hol and Spiers, 2012; Pan and Connell, 2007; Vandamme et al., 2010), where at higher CO₂ pressure (here: above ~4 MPa) poroelastic compression of the matrix significantly affects the measured swelling strains. Correcting the data of Day et al. (2008) for poroelastic effects (following Hol and Spiers, 2012), yields a roughly linear trend that extends down to ~0.2 mmol·g_{coal}⁻¹ (Fig. 11a). Despite the fact that superposition of adsorption-induced and poroelastic strains works well for high pressure data, the model is unsuccessful at very low concentrations, *i.e.* below ~0.2 mmol·g_{coal}⁻¹ in the data of Day et al. (2008). To date, no explanations exist for the “remaining strain offset”. We then took multiple swelling strain data sets for different samples reported in the literature (Astashov et al., 2008; Battistutta et al., 2010; Ceglarska-Stefanska and Czaplinski, 1991, 1993; Cui et al., 2007; Day et al., 2008; Hol and Spiers, 2012), and quantified the magnitude of the “remaining strain offset”. Only high pressure data ($P_f > 6$ MPa) by Hol and Spiers (2012), and Day et al. (2008) were corrected for linear poroelastic effects. Fig. 11b presents this offset as a function of the effective sample width (derived from the cube-root of the sample volume). Error bars represent worst case errors; in most cases linear fits could be made with $R^2 > 0.99$. The plot presented clearly shows that the remaining strain offset at low CO₂ concentrations appears to be the largest in bigger samples, and is closest to zero for samples with an effective width below the typical cleat spacing. This strongly suggests that the remaining strain offset correlates with sample size, and more general, that the presence of cleats in larger coal samples directly affects the measured bulk swelling strain. The effect is seen at low concentration/fluid pressure, and is evident in almost all data sets that report data on >cm-scale samples. The cube-shaped Prosper Haniel coal sample used in this study has an effective width of 80 mm, and therefore, its swelling behavior is expected to show a significant contribution of strain accumulated in the cleats (strain offset), possibly of the order of 0.6% volumetric strain for equilibration with CO₂.

To understand the inherent relation between the presence of cleats and strain during active loading, we focus in more detail on the role of surface roughness of cleat contacts, *i.e.* on the role of asperities. A primary reason for the presence of asperities at cleat contacts is heterogeneity. Coal macerals have different swelling properties (Milligan et al., 1997), which, can even lead to local strain differences within

the coal matrix (Karacan, 2003, 2007), and at surfaces (Brenner, 1983). We propose that the introduction of sorbing gases in cleat-bearing coal samples causes heterogeneous swelling of macerals along cleat interfaces, which alters the surface roughness of the matrix block between cleats. Because opposing matrix block surfaces will thereby misalign slightly, the normal stresses transmitted across the cleats will be intensified at specific asperities, and thus the effective mechanical stiffness will decrease. This mechanism is fully consistent with the idea of stress-dependent “cleat” compressibility (Connell et al., 2010; McKee et al., 1988; Shi and Durucan, 2004), only with the addition of a change in stress-dependence with type of sorbing fluid.

In the direction perpendicular to the bedding plane (vertical direction), the presence of cleats plays no role (assuming an ideal matchstick system), and hence strains must be associated with the mechanical behavior of macerals and microfractures only. In this vertical case, the abovementioned heterogeneous swelling of macerals may result in opening of pre-existing microfractures (Harpalani and Mitra, 2010; Massarotto et al., 2010), or the formation of new microfractures (Hol et al., 2012b). Previous studies indicate that the latter results in irreversible and slightly non-recoverable deformation, and frequently extends pre-existing cracks on the maceral boundaries in the bedding plane (Hol et al., 2012b). This may also explain the possible decrease in yield strength upon exposure to sorbing gases observed in some coal samples (Ranjith et al., 2010; Viete and Ranjith, 2006), and possibly not in others (Ates and Barron, 1988). The fractures formed, typically result in a hysteresis in swelling strain versus fluid pressure curves (Hol et al., 2012b; Moffat and Weale, 1955). We postulate that the increase in microfracture aperture and change in surface roughness after treatment with sorbing fluids will result in misalignment of bedding contacts, and hence more compliant behavior in the saturated and swollen state.

Although no microstructural analyses were performed on our sample to confirm the formation of cracks, we put forward two lines of evidence deduced from our mechanical data that support our claim. First, the magnitude of the strain anisotropy during loading was a clear function of the magnitude of the adsorption-related strain component at equilibrium (Fig. 9b). Recall, that “anisotropy” is defined here as the ratio of the vertical strain over the mean strain in the bedding plane ($2\Delta\varepsilon_v / (\Delta\varepsilon_{fc} + \Delta\varepsilon_{bc})$), and hence the consistent increase of anisotropy observed as a function of swelling strain at equilibrium (for different gases) suggest that the vertical strains directly relate to the swelling process itself. Contact mechanics at the cleat interface (horizontal) become of less relative importance in comparison with the direction perpendicular to the bedding after equilibration with sorbing gases. Second, the magnitude of the hysteresis in volumetric strain is mainly related to changes in the vertical strain component, and is consistently larger for the case where adsorption-related swelling strain is larger (Fig. 9c). Heterogeneous swelling-induced

microfracturing (disjoining bedding planes) is hence clearly consistent with the observed increase of elastic anisotropy. A possible reason for microfracturing manifesting itself most in the CO₂ equilibrated state is that the coal sample has been exposed to CH₄ in the in situ case, and is hence capable of accommodating initial heterogeneous swelling induced by the adsorption of CH₄.

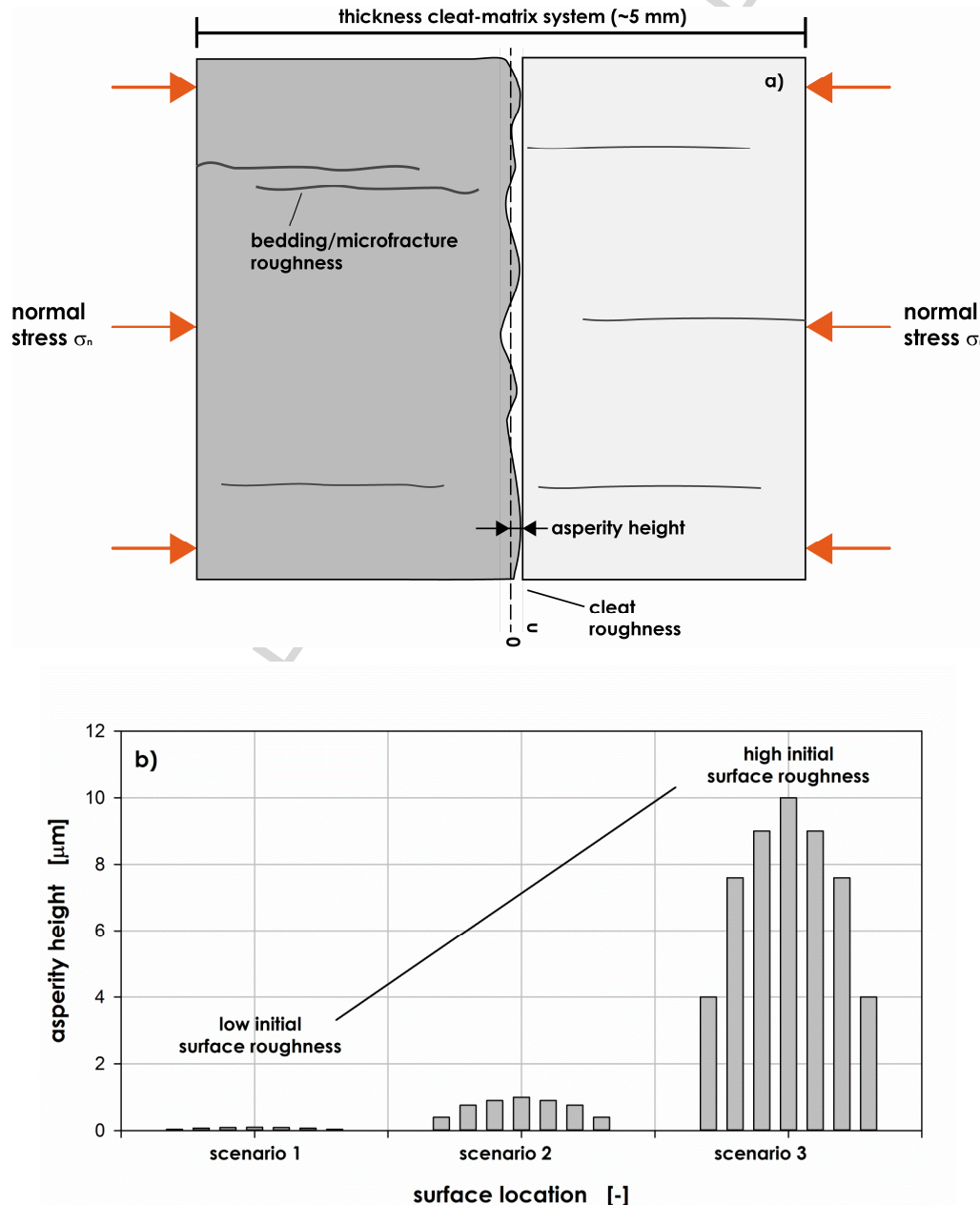


Fig. 12. a) Schematic of a rough contact between two coal matrix blocks separated by a cleat. The surface roughness of the contact is laterally repeatable. b) Distribution of initial asperity heights in three scenarios considered here.

On the basis of the above arguments, we propose that the bedding-parallel, swelling-induced microfracturing observed by others must have significantly contributed to the stress-strain hysteresis and reduction in stiffness seen in our coal sample in the direction perpendicular to the bedding, notably when exposed to CO₂. It is crucial to realize that strains related to compression of the swelling-induced microfractures can never be larger than the initial, maximum bulk swelling strain measured after equilibration, because the latter strain includes the strain associated with a maximum opening of the fractures. Comparing the mechanical data presented in Fig. 6 and Fig. 8 indeed shows that the compaction strains in the presence of sorbing gases (e.g. approximately 0.3% volumetric strain for CO₂) are smaller than their swelling strains (approximately 0.75% cumulative swelling strain for CO₂). Our mechanical data are hence fully consistent with the idea that microfracturing is responsible for the reduction in stiffness in the vertical direction.

To demonstrate that a) a change of asperity dimensions at cleat contacts (horizontal direction), and b) the formation of microfractures (vertical direction) can significantly contribute to the observed reduction in bulk stiffness, we adopt contact mechanics theory developed progressively by several authors (e.g. Almquist et al., 2011; Berthoud and Baumberger, 1998; Pastewka et al., 2013). The theory considers the frictionless contact between two elastic solids with a known stiffness. The surfaces of both solids have specific height profiles $h_0(x)$ and $h_1(x)$, which are effectively mapped as a single height profile $h(x)$ of a rigid substrate, in contact with an elastic solid. Please refer to Fig. 12a, modified from Almquist et al. (2011), for a schematic drawing of the situation considered. The total, one-dimensional bulk stiffness of the material is assumed to be a simple series of springs, obeying the expression,

$$K_{tot}^{-1} = K_1^{-1} + K_2^{-1} + K_i^{-1} \quad (1)$$

Focusing now on K_i , a generalization of the above yields that the interfacial stiffness can be expressed as (following Berthoud and Baumberger, 1998),

$$K_i = \frac{\sigma_{effn}}{u_0} \quad (2)$$

where σ_{effn} is the effective normal stress in MPa acting across the contact, and u_0 is the characteristic length in μm (see Fig. 12). The latter can be viewed as an explicit measure of surface roughness, which we write as a function of the root-mean-square of the average asperity height profile h_{rms} , and an empirical factor 0.4 (discussed in detail by Almquist et al., 2011),

$$u_0 = 0.4 \cdot h_{rms} = 0.4 \cdot \sqrt{\langle h(x, y) \rangle^2} \quad (3)$$

The surface roughness of our coal sample is expected to be small and the applied stresses high, so that the above theory is applicable to the problem considered here (refer to Pastewka et al., 2013 for an analytical

solution applicable to low normal stress). We now use Eq. 1-3 to evaluate the effect on interfacial stiffness of a small increase of surface roughness, and its subsequent contribution to the bulk modulus.

In applying the model, we assume a Gaussian distribution of initial asperity heights (Fig. 12b). These asperities themselves relate to the compositional heterogeneity. Three scenarios of initial maximum asperity amplitude h_{ini} are considered, namely: 0.1 μm , 1 μm , and 10 μm (Fig. 12b), and a fixed matrix modulus of 2.5 GPa. We insert the asperity distribution into Eq. 3 to obtain u_0 , and then calculate the interfacial stiffness K_i using Eq. 2. The total stiffness, both for the evacuated (initial) state ($K_{tot-ini}$), and the swollen state (K_{tot-s}), is then obtained using Eq. 1. The next step is to consider an increase in local asperity height, caused by heterogeneous swelling. The consequent reduction in one-dimensional stiffness ΔK_{tot}^* in % can be calculated from the stiffness in swollen state relative to the evacuated (initial) state, using the following, simple relationship,

$$\Delta K_{tot}^* = \left(\frac{K_{tot-s} - K_{tot-ini}}{K_{tot-ini}} \right) \cdot 100\% \quad (4)$$

Fig. 13 plots the reduction in (one-dimensional) stiffness, or modulus, as a function of increase in initial asperity amplitudes (Δh). The analytically obtained dependence shown in

Fig. 13 demonstrates that the three asperity height scenarios can all result in a significant reduction of bulk stiffness, which clearly supports the idea proposed in this section that small changes in asperity height induced by heterogeneous swelling or microfracturing can lead changes in bulk stiffness. Comparing now the three height scenarios considered in Fig. 12 and evaluated in

Fig. 13, we immediately recognize that the contact modulus of a specific surface with initially small roughness amplitude (low h_{max} , 0.1 μm in Fig. 12b) is most sensitive to changes in surface roughness. This implies that the stiffness of existing rough contact is less sensitive to a given change in roughness, than a new-formed, or existing smooth contact (compare cleat roughness with bedding/microfracture roughness - Fig. 12a). Our data show exactly this effect, namely the formation of microfractures in the bedding influences the vertical strain greater than the cleats do for the horizontal directions. Note, however, that the theoretical model used here drastically oversimplifies the true surface properties of cleat and fractures in coal material, their orientations, as well as the changes in induced in this by adsorption and swelling. Even so, we see that it is in semi-quantitative agreement with the experimental results reported, and we are therefore confident that our interpretation is valid. Swelling-induced changes in surface roughness at cleat interfaces and microfractures can significantly contribute to reducing the bulk modulus of coal.

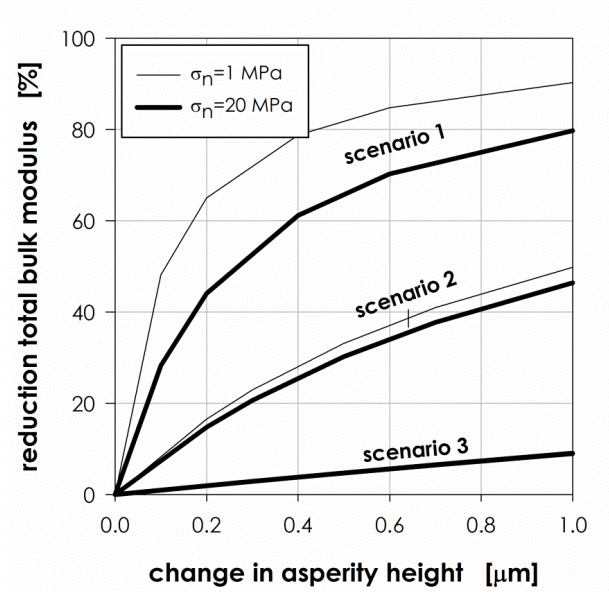


Fig. 13. Reduction in modulus versus change in asperity height, computed and plotted for the case where roughness at cleat surfaces is considered.

4.2.2 Mechanism 2: Thermodynamic coupling between stress state, adsorption capacity and swelling strain (maceral-scale)

The concentration profiles observed in the GC data (Fig. 5) suggest that fluid displacement and changes in gas composition in the Prosper Haniel sample were effectively completed in approximately 3 hours. This is in contrast with the time required to attain swelling equilibrium (30 hr for N₂ and CH₄, and 300 hr for CO₂ - Fig. 6). Moreover, the GC data showed continuous outgassing of residual N₂ and CH₄ during the CO₂ stage of the experiment. From this contrast in time and chemical composition profile, we infer that the first 3 hours of the GC data are dominated by flow and gas exchange in the face cleats only (recall from Section 2.2.1 that the fluid inlet and outlet ports were connected in the face cleat direction), and that equilibration of the complete sample occurred much later, due to diffusion through the matrix being 10 to 100 times slower the cleat flow rate. Any direct relationship between gas adsorption in the matrix and the mechanical response of the bulk sample is therefore expected to develop relatively slowly.

For the case of helium and CH₄, loading and unloading results in an almost instantaneous volumetric response (Fig. 10a and Fig. 10c). Time-dependent strain data recorded after N₂ equilibration were inconclusive, because of instability in the applied effective stress (recall Section 0), and after equilibration with helium, equilibrium is achieved in less than 1 hour. The quasi-instantaneous response is clearly in contrast with the behavior observed for CO₂ (Fig. 10d). Here, time-dependent strains can be observed for all loading steps, where equilibrium is not reached within the first hour. Furthermore, for the CO₂ equilibrated sample, unloading gives rise to enhanced swelling and loading to 12.5 MPa and 10.0 MPa to enhanced compaction. Similar time-dependent strain behavior, i.e. a time-dependent CO₂-related response contrasting with the behavior with He, was observed by Hol et al. (2011), and was described in terms of a direct coupling between stress state, adsorption capacity and swelling strain. Following, we will explore the potential contribution of this effect in determining the bulk modulus of our sample.

To demonstrate that the direct thermodynamic coupling between stress state, adsorption capacity and swelling strain can be related to apparent changes in the effective bulk stiffness of coal, we consider the theory developed by Hol et al. (2011), which states that

$$K_{matrix-app}^{-1} = K_{poro}^{-1} + K_{des}^{-1} = \frac{\epsilon_{poro} + \epsilon_{des}}{\sigma_e} \quad (5)$$

where the apparent stiffness $K_{matrix-app}$ in MPa is expressed as a function of the applied effective stress σ_e in MPa, the poroelastic strain ϵ_{poro} , and the stress-induced desorption strain (shrinkage) ϵ_{des} . The latter is further expressed as

$$\varepsilon_{des} = \frac{\Delta V_{des}}{V_{ini}} = \frac{\Omega_0 m_s}{V} C \left(1 - \frac{C_\sigma}{C} \right) \quad (6)$$

which represents the change in sample volume due to desorption ΔV_{des} over the initial sample volume V_{ini} in a swollen, stress-free state. The change in sample volume is further defined as a function of the apparent molecular volume of the sorbed phase Ω_0 in $\text{m}^3 \cdot \text{mole}^{-1}$, the mass of solid m_s in kg, and the sorbed concentration in the stress free state (C) and stressed states (C_σ). For the case where the sorbed concentration as a function of pressure is limited only by the change in chemical potential of the free fluid molecules, we can write the fractional reduction in sorption capacity due to the application of a compressive effective stress, i.e. the ratio C_σ/C in Eq. 6, as (cf. Hol et al., 2011),

$$\frac{C_\sigma}{C} \approx \exp\left(\frac{-\sigma_e \Omega_0}{kT}\right) \quad (7)$$

Here, we explicitly assume that the non-ideal nature of the adsorbate is the principal factor controlling the apparent saturation of the adsorbent, and that abundant adsorption sites are available. The above relationship (Eq.7) provides us with a direct thermodynamic coupling between external stress state σ_e and sorbed concentration C_σ in the matrix. Note, that the removal of fluid mass generates time-dependent shrinkage, which is controlled by the rate of diffusion and be observed volumetrically as creep (Hol et al., 2011; Hol et al., 2013). Conversely, re-adsorption and time-dependent swelling will occur upon unloading. In our data, 1) enhanced time-dependent compaction of the sample occurs while applying stress, after exposure to sorbing fluids, and 2) larger magnitudes of the compaction strains are observed in such as case (Fig. 10 and Fig. 8). From this we infer that, although most strain is occurring in the cleats and (probably new formed) fractures, direct fluid-matrix interaction effects are likely to play some role in the observed reduction in bulk coal stiffness. Note that, similar to the mechanism proposed in Section 4.2.1, the strains related to stress-induced desorption and shrinkage cannot be larger than the maximum bulk swelling strain measured after equilibration. This condition is also met.

Assuming a linear relationship between swelling and sorbed concentration, i.e. a fixed Ω_0 inferred from experimental data used as the basis for Fig. 11b, enables us to calculate the reduction of modulus over a particular stress range. Choosing effective stress conditions close to those applied in this study (we take $\sigma_e=0-20$ MPa), and an initial bulk modulus of 2.5 GPa at zero stress conditions, yields a reduction in bulk modulus of 3-15 % at 20 MPa of isostatic effective stress. This is significant, and of the order of the time-dependent strains we observed in our data. Note, however, that strongly swelling coal material at high effective stress will be more sensitive to the direct effect described here.

4.2.3 *Strain superposition and composite bulk modulus*

The above analyses demonstrate that both changes in surface roughness at cleat interfaces and microfractures, as well as the thermodynamic coupling between stress state, adsorption capacity and swelling strain can lead to a reduction of static bulk modulus. Both mechanisms lead to “apparent” changes in stiffness, in the sense that they are related to fluid-rock interactions and the presence of fractures rather than the inherent elastic properties of the solid phase itself. In the evacuated state, the matrix modulus has a fixed value, but in the fluid-equilibrated state it is represented as a composite property including the added surface roughness effect and the thermodynamic effect. Interestingly, the two mechanisms proposed in this study are operating at different scales (cleat- and bedding-scale versus the maceral scale). Hence, the strains associated with the different effects, and the resulting changes in moduli, may be treated as additive. A “composite” modulus and the changes thereto, can thus be obtained following the rationale presented by Eq. 1, taking into account the directionality in cleats and bedding features. In doing this, note that the change in matrix stiffness related to the thermodynamic coupling between stress state, adsorption capacity and swelling strain, occurs at the matrix-scale itself, and therefore alters the value of the matrix modulus used in Eq. 1, Section 4.2.1. As a consequence, the only correct scaling operation can be to go from the matrix scale to the formation scale, not vice versa.

4.3 **Upscaling to seam-scale geomechanics**

The morphology of coal layers is characterized by a cleat-matrix system, where multi-scale heterogeneity and anisotropy affect fluid transport and mechanical properties. We have considered the direct and indirect coupling between adsorption processes and the mechanical response of the bulk rock that can be seen in our laboratory data. An important remark should be made here on coal rank. The present study is performed using a high volatile bituminous coal sample, bearing a well-developed cleat system. Care should be taken when extrapolating our findings to lower rank coal, as structural features, including the developed cleat-matrix system, may be different.

Incorporating the underlying mechanisms reported here into reservoir simulations could clearly improve predictions of reservoir performance, despite the computational load. To do this most effectively, the relevance and importance of each mechanism must be assessed for the prediction of reservoir performance during CBM and ECBM.

Although further experimental work is required to constrain the stress, pressure and temperature conditions, their rank-dependence, as well as the scale of operation of the mechanisms proposed in this

study, the models are in strong agreement with the experimental observations reported. This leads to the general premise that for large, multi-cleat-bearing coal samples (as tested in this study), cleat density and aperture dominate the change in stiffness. Conversely, coal samples bearing few cleats, or subject to high stress states, will be affected strongly by direct, thermodynamic effects in the matrix. Although cleat aperture effects were overprinted in our study by microfracturing effects (Section 4.2.3), we expect that the true *in situ* relative importance of these two is opposite in effect; microfracturing has a significant effect on laboratory measurements conducted under constant stress state, but for many *in situ* cases, the initial stresses in the coal seam upon equilibration with the sorbing fluid will be sufficiently high to prevent opening of the fractures. We expect the effect of microfracturing on bulk stiffness, as seen in the experimental data reported here, as variable. Likely, cleats, which are naturally compliant, may reduce aperture under zero-strain (bulk) boundary conditions by heterogeneous swelling. We realize that this consideration raises questions on the direct applicability of laboratory data in predicting the *in situ* geomechanical response of coal seams. At the same time, this emphasizes the importance of identifying controlling mechanisms, both at the matrix-scale, as well as the multi-cleat/reservoir scale. The effect of stress on adsorption capacity and swelling strain is an example of a direct mechanism that we have identified at the smallest scale, i.e. the maceral-scale. The effect is of course dependent only on the extent of penetration of the adsorbate into the coal, but has a strong mechanical coupling with the *in situ* conditions, in particular when zero-strain boundary conditions are considered. Indeed, we note that the polyaxial cell at University Queensland can be operated at zero-strain boundary conditions (simulating a constant-volume reservoir), and future experiments can be performed in this mode to follow-up on our findings to date.

Finally, we note that other authors have proposed that plasticization of the macromolecular coal structure could be responsible for the reduction in bulk modulus of coal. However, we show here that solely mechanical and thermodynamic considerations at the larger scale, namely at the cleat- and maceral-scale, evidently offer less complicated explanations for the effect. Moreover, these two mechanisms are clearly supported by the appropriate theoretical/thermodynamic expressions. We therefore recommend to taking into account as primary operators of reservoir engineering simulators and geomechanical models only larger-scale mechanisms related to features such as heterogeneous bedding and cleats.

5 Conclusions

We have performed a single, long-duration mechanical experiment on a large, cube-shaped high volatile bituminous coal sample, under evacuated and helium-, N₂-, CH₄- and CO₂-equilibrated conditions. Using a mean gas pressure of 3 MPa, 3D strains, isotropic stresses, and fluid composition data, we have investigated direct mechanisms and feedback effects that sorbing fluids have on the recoverable mechanical response of bulk coal.

Our data showed that cyclic loading and unloading of the sample in the evacuated state resulted in non-linear, recoverable compaction. Exposure of the sample to He, N₂, CH₄ and CO₂, at 3 MPa fluid pressure and 6 MPa isostatic effective stress, lead to a subsequent volumetric swelling which depended strongly on the type of fluid sorbing (max. 0.05% for N₂ and 0.7% for CO₂). Although loading and unloading of the sample in the each fluid-equilibrated state resulted in a roughly similar recoverable strain response, the stress-strain trajectory followed in each case was characterized by strain hysteresis, stronger strain anisotropy, and lower bulk moduli. These effects were clearly dependent on the amount of cumulative swelling strain exhibited by the sample, with CO₂-sorption induced swelling resulting in the strongest increase in anisotropy (from 0.63 to 1.31) and hysteresis (from 0.05 to 0.15 volumetric strain), and highest reduction of the bulk modulus (~25%).

We conclude that the change in bulk modulus/stiffness observed in our sample is a combined effect of two, scale-dependent mechanisms; 1) changes in surface roughness at cleat interfaces (bedding-direction), and microfracturing (vertical direction), both caused by heterogeneous matrix swelling, and 2) a direct, thermodynamic coupling between stress state, adsorption capacity and swelling strain. Although these mechanisms are able to alter the measured stiffness/modulus of a coal sample at the bulk scale under laboratory conditions, the true *in situ* mechanical response of coal seams will be subjected to different boundary conditions. Our paper demonstrates the importance of identifying underlying controlling mechanisms to accurately predict the reservoir response during CBM and ECBM production.

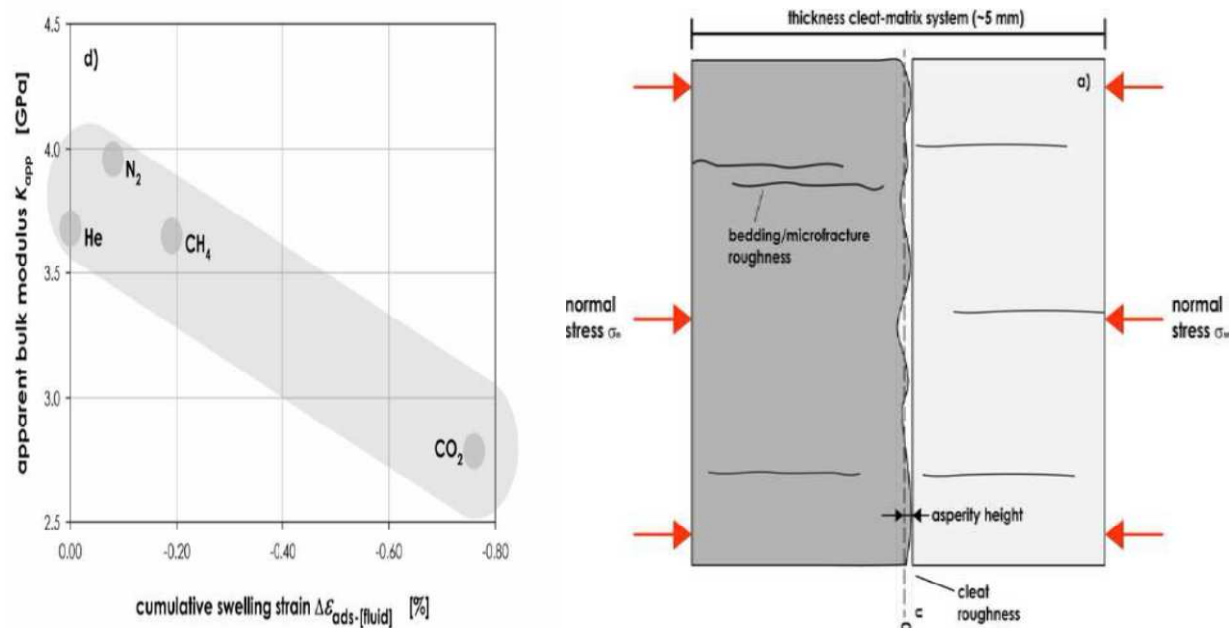
Acknowledgments

We thank Dean Biddle for his dedication in performing the experiments. Bernd Krooss, Christopher J. Spiers, and Lars Pastewka are thanked for the fruitful scientific discussions.

References

- Almqvist, A., Campaña, C., Prodanov, N., Persson, B.N.J., 2011. Interfacial separation between elastic solids with randomly rough surfaces: Comparison between theory and numerical techniques. *Journal of the Mechanics and Physics of Solids* 59, 2355-2369.
- Astakhov, A.V., Belyi, A.A., Bunin, A.V., 2008. Quasi-equilibrium swelling and structural parameters of coals. *Fuel* 87, 3455-3461.
- Ates, Y., Barron, K., 1988. The effect of gas sorption on the strength of coal. *Mining Science and Technology* 6, 291-300.
- Battistutta, E., van Hemert, P., Lutynski, M., Bruining, H., Wolf, K.-H., 2010. Swelling and sorption experiments on methane, nitrogen and carbon dioxide on dry Selar Cornish coal. *International Journal of Coal Geology* 84, 39-48.
- Berthoud, P., Baumberger, T., 1998. Shear stiffness of a solid–solid multicontact interface. *Proceedings of the Royal Society of London. Series A: Mathematical, Physical and Engineering Sciences* 454, 1615-1634.
- Brenner, D., 1983. In situ microscopic studies of the solvent-swelling of polished surfaces of coal. *Fuel* 62, 1347-1350.
- Busch, A., Gensterblum, Y., 2011. CBM and CO₂-ECBM related sorption processes in coal: A review. *International Journal of Coal Geology* 87, 49-71.
- Busch, A., Gensterblum, Y., Krooss, B.M., 2003. Methane and CO₂ sorption and desorption measurements on dry Argonne premium coals: pure components and mixtures. *International Journal of Coal Geology* 55, 205-224.
- Ceglarska-Stefanska, G., Czaplinski, A., 1991. The effect of limitation free expansion of hard coal on the sorption of carbon dioxide. *Archives of Mining Science* 36, 369-378.
- Ceglarska-Stefanska, G., Czaplinski, A., 1993. Correlation between sorption and dilatometric processes in hard coals. *Fuel* 72, 413-417.
- Connell, L.D., Lu, M., Pan, Z., 2010. An analytical coal permeability model for tri-axial strain and stress conditions. *International Journal of Coal Geology* 84, 103-114.
- Cook, N.G.W., 1992. Natural joints in rock: Mechanical, hydraulic and seismic behaviour and properties under normal stress. *International Journal of Rock Mechanics and Mining Sciences & Geomechanics Abstracts* 29, 198-223.
- Cui, X., Bustin, R.M., Chikatarla, L., 2007. Adsorption-induced coal swelling and stress: Implications for methane production and acid gas sequestration into coal seams. *Journal of Geophysical Research* 112, B10202.
- David, E.C., Brantut, N., Schubnel, A., Zimmerman, R.W., 2012. Sliding crack model for nonlinearity and hysteresis in the uniaxial stress–strain curve of rock. *International Journal of Rock Mechanics and Mining Sciences* 52, 9-17.
- Day, S., Fry, R., Sakurovs, R., 2008. Swelling of Australian coals in supercritical CO₂. *International Journal of Coal Geology* 74, 41-52.
- De Silva, P.N.K., Ranjith, P.G., 2012. Advanced core flooding apparatus to estimate permeability and storage dynamics of CO₂ in large coal specimens. *Fuel*.
- Gensterblum, Y., Busch, A., Krooss, B.M., 2014. Molecular concept and experimental evidence of competitive adsorption of H₂O, CO₂ and CH₄ on organic material. *Fuel* 115, 581-588.
- Gensterblum, Y., Ghanizadeh, A., Krooss, B.M., 2013a. Fluid-dynamical and poro-elastic coupling of gas permeability of inert gases on an Australian sub-bituminous coal. *Journal of Unconventional Oil and Gas Resources*.
- Gensterblum, Y., Merkel, A., Busch, A., Krooss, B.M., 2013b. High-pressure CH₄ and CO₂ sorption isotherms as a function of coal maturity and the influence of moisture. *International Journal of Coal Geology*.
- Gensterblum, Y., van Hemert, P., Billemont, P., Battistutta, E., Busch, A., Krooss, B.M., De Weireld, G., Wolf, K.H.A.A., 2010. European inter-laboratory comparison of high pressure CO₂ sorption isotherms II: Natural coals. *International Journal of Coal Geology* 84, 115-124.
- Gensterblum, Y., van Hemert, P., Billemont, P., Busch, A., Charrière, D., Li, D., Krooss, B.M., de Weireld, G., Prinz, D., Wolf, K.H.A.A., 2009. European inter-laboratory comparison of high pressure CO₂ sorption isotherms. I: Activated carbon. *Carbon* 47, 2958-2969.
- Gentzis, T., Deisman, N., Chalaturnyk, R.J., 2007. Geomechanical properties and permeability of coals from the Foothills and Mountain regions of western Canada. *International Journal of Coal Geology* 69, 153-164.
- Hagin, P.N., Zoback, M.D., 2010. Laboratory studies of the compressibility and permeability of low-rank coal samples from the Powder River Basin, Wyoming, USA, 44th U.S. Rock Mechanics Symposium and 5th U.S.-Canada Rock Mechanics Symposium, Salt Lake City, Utah.
- Harpalani, S., Mitra, A., 2010. Impact of CO₂ Injection on Flow Behavior of Coalbed Methane Reservoirs. *Transport in Porous Media* 82, 141-156.
- Hol, S., Peach, C.J., Spiers, C.J., 2011. Applied stress reduces the CO₂ sorption capacity of coal. *International Journal of Coal Geology* 85, 128-142.
- Hol, S., Peach, C.J., Spiers, C.J., 2012a. Effect of 3-D stress state on adsorption of CO₂ by coal. *International Journal of Coal Geology* 93, 1-15.
- Hol, S., Spiers, C.J., 2012. Competition between adsorption-induced swelling and elastic compression in coal at CO₂ pressures up to 100 MPa. *Journal of the Mechanics and Physics of Solids*.
- Hol, S., Spiers, C.J., Peach, C.J., 2012b. Microfracturing of coal due to interaction with CO₂ under unconfined conditions. *Fuel* 97, 569-584.
- Hol, S., Zoback, M. D., Spiers, C.J., 2013. Role of Adsorption in the Creep Behavior of Coal and Shale, *Poromechanics V*, Vienna, pp. 668-677.
- Jaeger, J.C., Cook, N.G.W., Zimmerman, R.W., 2007. *Fundamentals of Rock Mechanics*, 4 ed. Blackwell Publishing, Oxford.
- Karacan, C.O., 2003. Heterogeneous sorption and swelling in a confined and stressed coal during CO₂ injection. *Energy & Fuels* 17, 1595-1608.
- Karacan, C.O., 2007. Swelling-induced volumetric strains internal to a stressed coal associated with CO₂ sorption. *International Journal of Coal Geology* 72, 209-220.
- Liu, J., Chen, Z., Elsworth, D., Qu, H., Chen, D., 2011. Interactions of multiple processes during CBM extraction: A critical review. *International Journal of Coal Geology* 87, 175-189.
- Lwin, M.J., 2011. The effect of different gases on the ultrasonic response of coal. *Geophysics* 76, E155-E163.

- Masoudian, M.S., Airey, D.W., El-Zein, A., 2013. A chemo-poro-mechanical model for sequestration of carbon dioxide in coalbeds. *Geotechnique* 63, 235-243.
- Massarotto, P., Golding, S.D., Bae, J.S., Iyer, R., Rudolph, V., 2010. Changes in reservoir properties from injection of supercritical CO₂ into coal seams - A laboratory study. *International Journal of Coal Geology* 82, 269-279.
- McKee, C.R., Bumb, A.C., Koenig, R.A., 1988. Stress-dependent permeability and porosity of coal and other geologic formations. *SPE Formation Evaluation* March.
- Milligan, J.B., Thomas, K.M., Crelling, J.C., 1997. Solvent swelling of maceral concentrates. *Energy & Fuels* 11, 364-371.
- Moffat, D.H., Weale, K.E., 1955. Sorption by coal of methane at high pressures. *Fuel* 34, 449-462.
- Morcote, A., Mavko, G., Prasad, M., 2010. Dynamic elastic properties of coal. *Geophysics* 75, E227-E234.
- Palmer, I.D., Mansoori, J., 1998. How permeability depends on stress and pore pressure in coalbeds: A new model. *SPE Reservoir Evaluation & Engineering* December, 539-544.
- Pan, Z., Connell, L.D., 2007. A theoretical model for gas adsorption-induced coal swelling. *International Journal of Coal Geology* 69, 243-252.
- Pastewka, L., Prodanov, N., Lorenz, B., Müser, M.H., Robbins, M.O., Persson, B.N.J., 2013. Finite-size scaling in the interfacial stiffness of rough elastic contacts. *Physical Review E* 87, 062809.
- Ranjith, P.G., Jasine, D., Choi, S.K., Mehic, M., Shannon, B., 2010. The effect of CO₂ saturation on mechanical properties of Australian black coal using acoustic emission. *Fuel* 89, 2110-2117.
- Ranjith, P.G., Perera, M.S.A., 2012. Effects of cleat performance on strength reduction of coal in CO₂ sequestration. *Energy* 45, 1069-1075.
- Schuyer, J., Dijkstra, H., van Krevelen, D.W., 1954. Chemical structure and properties of coal VII - Elastic constants. *Fuel* 33, 409-418.
- Shi, J.Q., Durucan, S., 2004. Drawdown induced changes in permeability of coalbeds: A new interpretation of the reservoir response to primary recovery. *Transport in Porous Media* 56, 1-16.
- Skurtveit, E., Aker, E., Soldal, M., Angeli, M., Wang, Z., 2012. Experimental investigation of CO₂ breakthrough and flow mechanisms in shale. *Petroleum Geoscience* 18, 3-15.
- van Bergen, F., Spiers, C., Floor, G., Bots, P., 2009. Strain development in unconfined coals exposed to CO₂, CH₄ and Ar: Effect of moisture. *International Journal of Coal Geology* 77, 43-53.
- Vandamme, M., Brochard, L., Lecampion, B., Coussy, O., 2010. Adsorption and strain: The CO₂-induced swelling of coal. *Journal of the Mechanics and Physics of Solids* 58, 1489-1505.
- Viete, D.R., Ranjith, P.G., 2006. The effect of CO₂ on the geomechanical and permeability behaviour of brown coal: Implications for coal seam CO₂ sequestration. *International Journal of Coal Geology* 66, 204-216.
- Viete, D.R., Ranjith, P.G., 2007. The mechanical behaviour of coal with respect to CO₂ sequestration in deep coal seams. *Fuel* 86, 2667-2671.
- Walsh, J.B., 1965. The effect of cracks on the uniaxial elastic compression of rocks. *Journal of Geophysical Research* 70, 399-411.
- Wang, F.Y., Zhu, Z.H., Massarotto, P., Rudolph, V., 2007. Mass transfer in coal seams for CO₂ sequestration. *AIChE Journal* 53, 1028-1049.
- Wang, G.X., Wei, X.R., Wang, K., Massarotto, P., Rudolph, V., 2010. Sorption-induced swelling/shrinkage and permeability of coal under stressed adsorption/desorption conditions. *International Journal of Coal Geology* 83, 46-54.
- White, C.M., Smith, D.H., Jones, K.L., Goodman, A.L., Jikich, S.A., LaCount, R.B., DuBose, S.B., Ozdemir, E., Morsi, B.I., Schroeder, K.T., 2005. Sequestration of carbon dioxide in coal with enhanced coalbed methane recovery - A review. *Energy & Fuels* 19, 659-724.
- Zimmerman, R.W., 1985. The effect of microcracks on the elastic moduli of brittle materials. *Journal of Materials Science Letters* 4, 1457-1460.
- Zisman, W.A., 1933. Compressibility and anisotropy of rocks at and near the earth's surface. *Proceedings of the National Academy of Sciences of the United States of America* 19, 666-679.



Graphical abstract

Research highlights

- CO₂-swollen coal exhibits stress-strain hysteresis, strain anisotropy and decrease in modulus.
- Swelling-induced changes of internal surface roughness changes modulus.
- Thermodynamic coupling stress state, sorption capacity and swelling strain changes modulus.
- Changes in modulus not related to inherent elastic properties of the solid phase.

ACCEPTED MANUSCRIPT